Heriot-Watt University
Research Gateway

Wind and current effects on extreme wave formation and breaking

Citation for published version:
Zou, Q & Chen, H 2017, 'Wind and current effects on extreme wave formation and breaking', *Journal of Physical Oceanography*, vol. 47, no. 7, pp. 1817-1841. https://doi.org/10.1175/JPO-D-16-0183.1

Digital Object Identifier (DOI):
10.1175/JPO-D-16-0183.1

Link:
Link to publication record in Heriot-Watt Research Portal

Document Version:
Publisher's PDF, also known as Version of record

Published In:
Journal of Physical Oceanography

Publisher Rights Statement:
© 2018 American Meteorological Society (AMS). Permission to use figures, tables, and brief excerpts from this work in scientific and educational works is hereby granted provided that the source is acknowledged. Any use of material in this work that is determined to be “fair use” under Section 107 of the U.S. Copyright Act or that satisfies the conditions specified in Section 108 of the U.S. Copyright Act (17 USC §108) does not require the AMS’s permission.

General rights
Copyright for the publications made accessible via Heriot-Watt Research Portal is retained by the author(s) and / or other copyright owners and it is a condition of accessing these publications that users recognise and abide by the legal requirements associated with these rights.

Take down policy
Heriot-Watt University has made every reasonable effort to ensure that the content in Heriot-Watt Research Portal complies with UK legislation. If you believe that the public display of this file breaches copyright please contact open.access@hw.ac.uk providing details, and we will remove access to the work immediately and investigate your claim.

Download date: 05. May. 2023

Wind and Current Effects on Extreme Wave Formation and Breaking

QINGPING ZOU AND HAIFEI CHEN

Department of Civil and Environmental Engineering, University of Maine, Orono, Maine

(Manuscript received 22 August 2016, in final form 11 March 2017)

ABSTRACT

Wind and current effects on the evolution of a two-dimensional dispersive focusing wave group are investigated using a two-phase flow model. A Navier–Stokes solver is combined with the Smagorinsky subgrid-scale stress model and volume of fluid (VOF) air–water interface capturing scheme. Model predictions compare well with the experimental data with and without wind. It was found that the following and opposing winds shift the focus point downstream and upstream, respectively. The shift of focus point is mainly due to the action of wind-driven current instead of direct wind forcing. Under strong following/opposing wind forcing, there appears a slight increase/decrease of the extreme wave height at the focus point and an asymmetric/symmetric behavior in the wave focusing and defocusing processes. Under a weak following wind, however, the extreme wave height decreases with increasing wind speed because of the dominant effect of the wind-driven current over direct wind forcing. The vertical shear of the wind-driven current plays an important role in determining the location of and the extreme wave height at the focus point under wind actions. Furthermore, it was found that the thin surface layer current is a better representation of the wind-driven current for its role in wind influences on waves than the depth-uniform current used by previous studies. Airflow structure above a breaking wave group and its link to the energy flux from wind to wave as well as wind influence on breaking are also examined. The flow structure in the presence of a following wind is similar to that over a backward-facing step, while that in the presence of an opposing wind is similar to that over an airfoil at high angles of attack. Both primary and secondary vortices are observed over the breaking wave with and without wind of either direction. Airflow separates over the steep crest and causes a pressure drop in the lee of the crest. The resulting form drag may directly affect the extreme wave height. The wave breaking location and intensity are modified by the following and opposing wind in a different fashion.

1. Introduction

Extreme waves, often referred to as rogue or freak waves, are single giant waves that are more than twice the size of what is expected for a given sea state. They are rare and unexpected events that can pose a threat to offshore operations and maritime activities.

Several physical mechanisms have been proposed for the formation of freak waves (Kharif and Pelinovsky 2003). Among them, the spatiotemporal focusing due to the dispersion of water waves is one mechanism that can produce abnormally large waves over a small area within a short period of time. Although occasionally freak waves occur during good weather conditions with light wind, freak waves are often accompanied by strong wind (e.g., Mori et al. 2002). Wind blows over the sea surface and exchanges momentum and energy with surface waves through air–sea interaction. Currently there is a lack of studies of the effect of wind and vertical current shear on the formation and breaking of freak waves. The literature of opposing wind influences is even more scarce; therefore, our understanding of the effect of opposing wind on the air–sea interaction with and without breaking remains elusive.

In the past decades, extensive experimental studies have been conducted to investigate wind-generated waves and the influence of wind on the growth and decay of mechanically generated water waves (Dobson 1971; Elliott 1972; Snyder et al. 1981; Mitsuyasu and Honda 1982; Banner and Peirson 1998; Hristov et al. 2003; Peirson and Banner 2003; Mitsuyasu and Yoshida 2005; Donelan et al. 2006; Peirson and Garcia 2008; Savelyev et al. 2011). One particular concern in these observations is to determine the criterion for airflow separation to occur over the waves. Banner and Melville (1976) argued that the airflow separation occurs only in the presence of breaking waves because in the reference frame that propagates with the wave, separation occurs at the stagnation point on the interface, which corresponds to the onset of breaking. Weissman (1986) and

Corresponding author: Qingping Zou, qingping.zou@maine.edu

DOI: 10.1175/JPO-D-16-0183.1

© 2017 American Meteorological Society. For information regarding reuse of this content and general copyright information, consult the AMS Copyright Policy (www.ametsoc.org/PUBSReuseLicenses).

Tian et al. (2010), however, observed airflow separations over nonbreaking short waves. Through experimental studies, Banner (1990) found that the presence of actively breaking waves enhanced the pressure phase shift, the form drag, and the wind stress. Recent development of the digital particle image velocimetry (DPIV) technique provides insights into the instantaneous airflow separation above the short gravity breaking wave groups (Reul et al. 1999, 2008). Buckley and Veron (2016) observed airflow separation above wind waves but not above mechanically generated swell.

Recently, Giovanangeli et al. (2005), Touboul et al. (2006), and Kharif et al. (2008) conducted laboratory experiments of the following wind effects on freak waves. Their studies indicated that the following wind shifts the focus point downstream and increases the peak wave amplitude. They also found that extreme wave events sustain longer due to the airflow separation on the leeward side of the steep crests and the wind-induced current. Qualitative agreements were achieved between their numerical models based on a boundary integral equation method and Jeffreys' sheltering theory and experiments for wave groups with large steepness where spilling breakers occurred under strong wind (Kharif et al. 2008). Tian and Choi (2013) investigated the following wind effect on two-dimensional dispersive focusing wave groups experimentally in a wave flume and numerically through a pseudospectral wave model. The wind forcing was represented using Miles' shear instability theory (Miles 1957, 1993) and Jeffreys' sheltering model (Jeffreys 1925), whereas the wave breaking–induced dissipation was incorporated through an eddy viscosity model. It was found that the model predicts the observations satisfactorily for weak wind by including the effect of wind-induced current. The model performance, however, deteriorates for strong wind forcing.

Air–sea interaction and breaking waves in deep water have been studied extensively in the past decades (Perlin et al. 2013). Notable theoretical work includes Jeffreys (1925), Miles (1957, 1993), Phillips (1957), Janssen (1991), and Belcher and Hunt (1993). Jeffreys (1925) proposed that the wave growth is due to the asymmetric pressure distribution caused by the airflow separation behind the wave crests. Miles (1957) developed a critical layer theory of wind waves based on linear stability analysis of a stratified shear flow. The wave-induced perturbation in the airflow grows dramatically near the critical height where the wind speed equals the wave propagation speed. The energy and momentum at the critical height in turn are transferred to the surface wave. The wave growth rate was found to be proportional to the curvature to slope ratio of the wind profile at the critical height. Phillips (1957) suggested that the wave growth at the initial stage is generated by the resonance between atmospheric turbulence pressure fluctuations and perturbation of water surface. The Miles' theory for wind-wave growth was later extended by Miles (1962), Phillips (1977), Janssen (1991), and Miles (1993) to include viscous and turbulent effects and validated in the field by Hristov et al. (2003) and in the laboratory by Grare et al. (2013). Belcher et al. (1993) used the truncated mixing length model to develop an analytical expression for the leading-order energy flux from atmosphere to wave motions and found significant wave growth generated by asymmetric pressure around the wave crest due to a nonseparated sheltering effect. Belcher and Hunt (1998) further examined the relative importance of the nonseparated sheltering effect and critical layer in momentum transfer from wind to wave for relatively slow and fast waves and waves with intermediate propagation speed. Zou (1998) applied a viscoelastic turbulent closure model and used three-layer matched asymptotic expansions to derive the analytical solutions for the turbulent flow over undulating topography with mild slopes. It was found that the Reynolds shear stress oscillates with the distance from the surface, and it contributes to the drag force at the same order as the asymmetric pressure. The theory of turbulent flow over a hill was extended to turbulent flow over progressive water waves by Zou (1995). A fair agreement was found between wave growth rate predicted by the theory and Plant's (1982) compilation of observation data (cf. Zou 1995, chapters 1, 8).

Numerical modeling of wind effects on extreme waves has been largely one-phase models. In the one-phase model of the marine atmospheric boundary layer, it has been a common practice to treat the free surface of the wave field as a wavy surface moving at a specified speed and simulate only the airflow motion above the wavy surface (Belcher et al. 1993; Zou 1998; Sullivan et al. 2000, 2007, 2008; Yang and Shen 2010, 2011; Hara and Sullivan 2015). In the one-phase ocean wave model, however, the water wave motion is modeled without coupling directly with the airflow (Chen et al. 2004; Touboul et al. 2006; Kharif et al. 2008; Chambarel et al. 2010; Yan and Ma 2011; Tian and Choi 2013; Liu et al. 2015). The wind effects are incorporated based on Miles' shear flow instability theory (Miles 1957, 1993), Jeffreys' sheltering hypothesis (Jeffreys 1925), or other empirical models that parameterize the momentum and energy exchange between the wind and wave. Overall, these one-phase models capture either the air or water flow but not both and must therefore rely on an empirically parameterized one-way coupling from wave to wind. The two-phase flow model is a more physics-based approach that avoids empirical parameterizations by simulating the air and water motion simultaneously. These

models can directly simulate violent dynamic events such as breaking waves, and they allow for a two-way dynamic wind/wave coupling.

Two types of numerical treatments have been adopted to capture the air–water interface in two-phase models. In the first type of two-phase models, the Navier–Stokes equations are solved in the air and water domain separately, and the predicted air and water flow are coupled by enforcing the continuity of velocity and balance of stress at the air–water interface (Fulgosi et al. 2003; Lin et al. 2008; Yang and Shen 2011). The modeling grid is boundary fitted and remeshed with time to follow the moving interface, with fine resolution near the interface to resolve the adjacent boundary layers in the air and water side. This type of model is suitable for viscous airflow over waves with moderate steepness. It is not applicable when wave breaking occurs and gives rise to large and violent deformation of the interface, entrainment of one fluid into the other, fluid fragmentation, and coalescence (Lakehal et al. 2002; Fulgosi et al. 2003).

In the second type of two-phase models, the Navier–Stokes equations are solved in both air and water computational domain on a fixed Eulerian mesh, with the two phases treated as one fluid so that the continuity of velocity and balance of stress are satisfied by default at the interface (Yan and Ma 2010; Hieu et al. 2014; Xie 2014). The air water interface is captured by the volume of fluid (VOF) method (Hirt and Nichols 1981; Scardovelli and Zaleski 1999), the level set method (Sethian and Smereka 2003; Wang et al. 2009; Zhang et al. 2010a,b), or a coupled VOF and level set method (Sussman et al. 2007; Lv et al. 2009, 2010, 2012). These methods are particularly robust to capture the large and complex topological changes of the interface associated with breaking waves. They are therefore adopted in the present study of wind influences on freak waves.

Recently, Iafrati et al. (2013) used 2D direct numerical simulation (DNS) of the Navier–Stokes equations for air and water two-phase flow to study the deep-water wave breaking induced by modulational instability without the presence of external wind and its contribution to the air–sea interaction. Contrary to expectations, they found that the energy dissipation in air is greater than that in water. This raises questions about the current parameterizations of wave breaking–induced dissipation in both deep and shallow waters based on the amount of energy dissipated in the water only.

Most two-phase models of wind-wave interactions adopt the VOF surface capturing method. Hieu et al.'s (2014) Reynolds-averaged Navier–Stokes (RANS)–VOF model results suggested that the wave overtopping at a sloping seawall is strongly affected by the wind. Xie (2014) used a two-phase RANS–VOF model to investigate the following wind effect on breaking solitary waves and found that the maximum runup height increases with the wind speed in the same direction as the wave. Lacking experimental results in the presence of wind, these two models were validated only for cases without wind. Yan and Ma (2010) nested a potential flow model [Quasi Arbitrary Lagrangian-Eulerian Finite Element Method (QALE-FEM)] with VOF-based commercial software StarCD to examine the interaction between wind and 2D freak waves and compared with the measured peak wave height in the presence of wind. But the model–data comparisons of the time history of surface elevation were not presented.

Part of the momentum from wind is transferred into the wave motion through the pressure force exerted on the air–water interface, while the other part is transferred to the near-surface current through the tangential friction force at the interface (Savelyev et al. 2011). Therefore, both direct wind forcing and wind-driven currents dictate how the wind affects the evolution of a wave group. Banner and Song (2002) investigated numerically the onset of wave breaking for a modulating wave group under the action of a following wind and a following current with uniform vertical shear at the free surface. It was found that the presence of a surface shear accelerates the onset of breaking and that the surface shear tends to modify the wave profiles more strongly than the direct wind forcing.

The effect of wind-induced surface current shear on the evolution of a dispersive focusing wave group, however, has not been studied previously. Although the wind-driven current is by no means uniform across the water depth, it has been a common practice to assume a depth-uniform wind-induced current profile in the previous studies of wind effect on waves (Touboul et al. 2006; Kharif et al. 2008; Chambarel et al. 2010; Yan and Ma 2011; Tian and Choi 2013). Neglecting the direct wind forcing, Moreira and Chacaltana (2015) used a fully nonlinear boundary integral method to examine the wind-driven, nonuniform current effects on wave transformations in deep water. Their results show that current shear may enhance wave blocking/breaking.

The objective of the paper is to examine the wind influence on the evolution of a breaking and nonbreaking dispersive focusing wave group using a two-phase flow model, with special attention to opposing wind, which has been hardly studied before. In particular, the contribution of the wind-driven current including surface shear is analyzed to examine its importance relative to direct wind forcing. The model results are validated with the experimental data with and without following wind. The opposing wind effect on the wave group's evolution is then studied to assess the effect of wind direction. After the introduction in section 1, the mathematical formulation

and numerical method for the two-phase flow model are described in section 2. The setup of the numerical wind-wave tank is illustrated in section 3. The model results and discussions are given in section 4. More discussions on the mechanism of wind effect on the wave group evolution are presented in section 5 based on additional model results. Airflow structures above a breaking and nonbreaking focusing wave group in the presence of following/opposing wind are investigated. Conclusions are drawn in section 6.

2. Model descriptions

a. Governing equations

The air and water motion is assumed to be governed by the Navier–Stokes equations for an incompressible fluid. Since only one set of mass and momentum conservation equations is used for both the air and water phases, the equations have to account for the material properties and the surface tension force at the air–water interface. The mass conservation and Navier–Stokes momentum equations are given by

$$\nabla \cdot \mathbf{U} = 0, \tag{1}$$

$$\frac{\partial \rho \mathbf{U}}{\partial t} + \nabla \cdot (\rho \mathbf{U}\mathbf{U}) - \nabla \cdot (\mu_{\text{eff}} \nabla \mathbf{U}) = -\nabla p^* - \mathbf{g} \cdot \mathbf{X} \nabla \rho + \nabla \mathbf{U} \cdot \nabla \mu_{\text{eff}} + \sigma \kappa \nabla \alpha, \tag{2}$$

where $\mathbf{U}$ is the velocity vector, ρ is the fluid density, p^* is the pseudodynamic pressure, $\mathbf{g}$ is the gravitational acceleration, $\mathbf{X}$ is the position vector, σ is the surface tension coefficient, κ is the free-surface curvature, α is the volume fraction to be introduced later, and $\mu_{\text{eff}} = \mu + \rho\nu_t$ is the effective dynamic viscosity, which takes into account of the molecular dynamic viscosity μ and the turbulent eddy viscosity ν_t.

The same set of governing equations listed above is solved simultaneously throughout the domain, considering both the air and water as one effective fluid. The VOF function in a fixed cell α is used as an indicator function to mark the location of the air–water interface. The interface is not defined as a sharp boundary but a transition region where the fluid is treated as a mixture of the two fluids. The VOF function $\alpha = 1$ if the cell is full of water, $\alpha = 0$ if the cell is full of air, and $0 < \alpha < 1$ if the cell is a mixture of air and water. The local density ρ and the local viscosity μ of the fluid are given by

$$\rho = \alpha\rho_1 + (1 - \alpha)\rho_2, \quad \text{and} \tag{3}$$

$$\mu = \alpha\mu_1 + (1 - \alpha)\mu_2, \tag{4}$$

where the subscripts 1 and 2 denote the variables for water and air, respectively.

The scalar field of the VOF function is described by the advection equation (Weller 2005)

$$\frac{\partial \alpha}{\partial t} + \nabla \cdot (\mathbf{U}\alpha) + \nabla \cdot [\mathbf{U}_r \alpha(1 - \alpha)] = 0, \tag{5}$$

where an extra compression term $\nabla \cdot [\mathbf{U}_r\alpha(1 - \alpha)]$ is added to the conventional VOF transport equation to limit the smearing of the interface (Hirt and Nichols 1981). This artificial convective term is active only in the thin interface region because the multiplication term $a(1 - \alpha)$ vanishes when $\alpha = 1$ (water side) or $\alpha = 0$ (air side). The quantity $\mathbf{U}_r$ is a velocity field used to compress the interface, which is calculated based on the local velocity in the interface region. More details about the relative velocity $\mathbf{U}_r$ and the VOF interface capturing method can be found in Rusche (2002) and Berberović et al. (2009).

b. Turbulence modeling

Only one set of conservation equations is used in the air–water two-phase flow solver in this study. Accordingly, a single turbulence model is applied for both air and water phases. In the spirit of large-eddy simulation (LES), the Navier–Stokes equations are spatially low-pass filtered such that the large, energy carrying eddies are resolved by the Navier–Stokes solver and the unresolved, small-scale, dissipative eddies are represented by a subgrid-scale (SGS) stress model. In the present study, the standard Smagorinsky model is used (Smagorinsky 1963). Assuming that the energy production and dissipation of the small-scale eddies are in equilibrium, the turbulent eddy viscosity can be expressed as

$$\nu_t = (C_s\Delta)^2|S|, \tag{6}$$

where C_s is the Smagorinsky constant with a default value of 0.167, Δ is the filter size, and $|S| = \sqrt{2S_{ij}S_{ij}}$ is the magnitude of the strain rate tensor $S_{ij} = 1/2(\partial u_i/\partial x_j + \partial u_j/\partial x_i)$.

c. Two-phase flow solver

Open Field Operation and Manipulation (OpenFOAM) is an open-source software for the solution of continuum mechanics problems, computational fluid dynamics (CFD) in particular. It is written in C++ and has a modular code structure that allows the users to add new solvers and utilities without delving into the source code. It has built-in support for many technical aspects including parallelization, mesh modifications and motion, and turbulence modeling (Weller et al. 1998).

For free-surface Newtonian flows, OpenFOAM contains a standard solver, interFoam, for solving the Navier–Stokes equations for two incompressible phases.

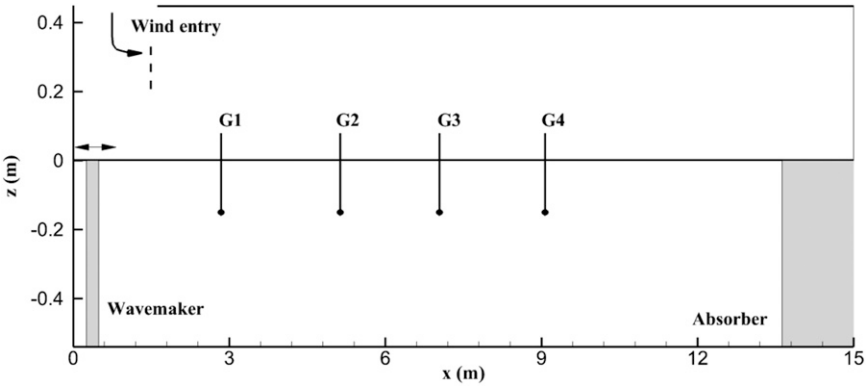

FIG. 1. Sketch of the 2D experimental wind and wave flume in Tian and Choi (2013) and the coordinate system in the present study, where the four gauges, G1–G4, for surface elevation measurements are indicated. The surface elevation measurement at G1 is used to drive the wavemaker for the present two-phase flow model.

The solver uses a finite-volume discretization and the VOF surface capturing method. Equations (1)–(6) are solved using the Pressure Implicit with Splitting of Operators (PISO) algorithm. The readers are referred to Jasak (1996) for a detailed description of OpenFOAM implementation. An extended version of the two-phase flow solver, waves2Foam (Jacobsen et al. 2012), is adopted in this study to investigate the wind-wave interaction. The waves2Foam solver includes water wave generation and absorption using the relaxation zone technique.

3. Model setup

a. Physical test

Two-dimensional wind and wave experiments were conducted by Tian and Choi (2013) in a 15-m-long, 1.5-m-wide, and 0.54-m-deep wave flume. Surface elevations at a sequence of wave gauge stations along the tank were measured with high-speed imaging techniques. As illustrated in Fig. 1, the measurements at four wave gauge (G1–G4) locations are used in the present study to evaluate the performance of the two-phase flow model. The dispersive focusing wave group was generated by a piston-type wavemaker. At the inlet of the flume, a twin-fan blower was used to generate the following wind above the wave flume. The ceiling panel of the air passage is 0.45 m above the still water surface during the experiments. At the outlet of the flume, a wave absorber made of loose nets and stainless steel grids is used to minimize the wave reflection.

The dispersive focusing wave group in Tian and Choi's (2013) experiment has a frequency band ranging from 1.0 to 2.4 Hz, with a peak frequency of 1.1 Hz and center frequency of 1.7 Hz. The wave steepness for each of the $N = 128$ components was kept constant. The two wave groups referred as DF 1 and DF 2 in Table 1 of Tian and Choi (2013) were tested. The DF 1 wave group with a global wave steepness $\varepsilon = Na_nk_n$ equal to 0.25 remains nonbreaking under all wind forcing conditions; the DF 2 wave group with $\varepsilon = Na_nk_n$ equal to 0.57 exhibits a plunging breaker in the absence of wind. We will focus on the nonbreaking wave group DF 1 in the majority of this paper and provide the model results for breaking wave group (DF 2) at the end of the paper to highlight the effect of breaking in this problem.

b. Numerical wind-wave tank setup

A 2D numerical wave tank (NWT) was developed to reproduce the physical test. The domain of the NWT starts at wave gauge G1 and ends at the outlet of the physical tank. The computational domain is thus 12.16 m long and 0.99 m high, including both air and water. The same global coordinate system as that in Tian and Choi (2013) is used. It is defined such that the x axis is positive in the direction of wave propagation, with $x = 2.84$ m at wave gauge G1, and the z axis is positive upward, with $z = 0$ at the mean water level and $z = -0.54$ m at the bottom (see Fig. 1). The computational domain is meshed with a uniform grid size of 0.0132 m first. In the vicinity of the free surface, the base mesh is then refined twice to obtain a finer mesh size of 0.0033 m. The time step is automatically adjusted according to the maximum Courant number limit of 0.25.

c. Boundary conditions

The inlet boundary of the model is located at the wave gauge G1, where the measured wave surface elevation of a dispersive wave group is used to drive the model. The time history of surface elevation at G1 is first

transformed into the frequency domain using the fast Fourier transform (FFT) and then reconstructed with $N = 128$ linear wave components:

$$\eta(x,t) = \eta_m + \sum_{n=1}^{N} a_n \cos[\omega_n t - k_n(x - x_m) + \varepsilon_n] + c.c., \tag{7}$$

where η is the surface elevation, *c.c.* denotes the complex conjugate, η_m is the mean surface elevation, a_n is the nth wave component amplitude, ω_n is the radian frequency, k_n is the wavenumber, ε_n is the phase shift, and x_m is the position of the wave gauge G1. The wavenumber k_n is obtained by the linear dispersion relation in the absence of a current $\omega_n^2 = gk_n \tanh(k_n d)$, where g is the gravitational acceleration, and d is the water depth. The long waves at the back of a wave group propagate faster than the short waves in the front of the wave group due to wave dispersion, thus the individual wave components become in phase with each other at a particular spatial location where the peak wave occurs. This location of the peak wave is called the focus point.

The water particle velocities at the inlet are calculated using the linear wave theory:

$$u_w(x,z,t) = \sum_{n=1}^{N} a_n \omega_n \frac{\cosh[k_n(z+d)]}{\sinh k_n d} \times \cos[\omega_n t - k_n(x - x_m) + \varepsilon_n] + c.c., \quad \text{and} \tag{8}$$

$$w_w(x,z,t) = \sum_{n=1}^{N} -a_n \omega_n \frac{\sinh[k_n(z+d)]}{\sinh k_n d} \times \sin[\omega_n t - k_n(x - x_m) + \varepsilon_n] + c.c., \tag{9}$$

where u_w and w_w are the horizontal and vertical velocity of wave motion. In the presence of a vertically varying current $U_c(z)$, a superposition of the wave and the current velocity is specified as the water particle velocity at the inlet:

$$u(x,z,t) = u_w(x,z,t) + U_c(z). \tag{10}$$

The wind entry is specified at the same location as the wavemaker. As no measurement was made at this location, the uniform wind profile is applied for the air phase at the inlet. The lowest grid point of wind forcing moves up and down with the water surface elevation. If the lowest point of wind forcing is too close to the water surface, the wave profile at the inlet may be distorted under high wind speeds. With this in mind, Xie (2014) chose to impose no wind forcing within a distance of about five grids above the water surface at the wavemaker. In the present study, we adopt a different approach by specifying a short relaxation zone for wind and waves at the inlet. It allows a smooth transition from the target incident waves at the wavemaker to downstream wind-affected waves and avoids significant distortion due to the wind forcing at the inlet.

At the outlet boundary, another relaxation zone is used to smoothly dissipate the wave motion without changing the airflow. To achieve this, a new relaxation scheme is added to the waves2Foam framework by Jacobsen et al. (2012). The inlet current profile is adopted at the outlet to maintain mass conservation. A zero gradient boundary condition is applied for the airflow at the outlet. The top and bottom boundaries of the computational domain are treated as rigid walls where the law of the wall is applied.

d. *Initial conditions*

Without wind, the wind and wave field is initialized from a still water condition, with zero velocity for both the air and water. In the presence of wind, the velocity in the air is initialized with the same steady wind profile along the wind-wave tank. Since the wave height is very small in the first 10 s, the wind-driven current and wind forcing may have sufficient time to develop. When it comes to examine the separate wind-driven current effect, the velocity in the water is initialized with a steady vertical current profile that may be either uniform across the water depth or exponentially sheared within a thin layer below the water surface.

4. Results and discussions

a. *Evolution of the wave group without wind*

Figure 2 shows that the present model results agree very well with the experimental data and the prediction by the pseudospectral wave model in Tian and Choi (2013). The wave group is generated at gauge G1 and reaches the peak wave height at the focus point around gauge G3. Downstream from this point, the amplitude of the group decreases rapidly as the long waves start to lead the wave group and outrun the short waves, and individual wave components become out of phase with each other.

b. *Evolution of the wave group under following wind*

As in the experiment, three following wind speeds $U_0 = 1.4$, 3.2, and 5.0 m s^{-1} are simulated. Figure 3 shows the evolution of the wave group under a wind speed of $U_0 = 3.2$ m s^{-1}. As the measurement at gauge G1 is used to drive the model, there is a perfect match at this gauge. Starting at gauge G2, the wind effect comes into play, and slight differences appear between the present simulation, the experimental data, and the numerical

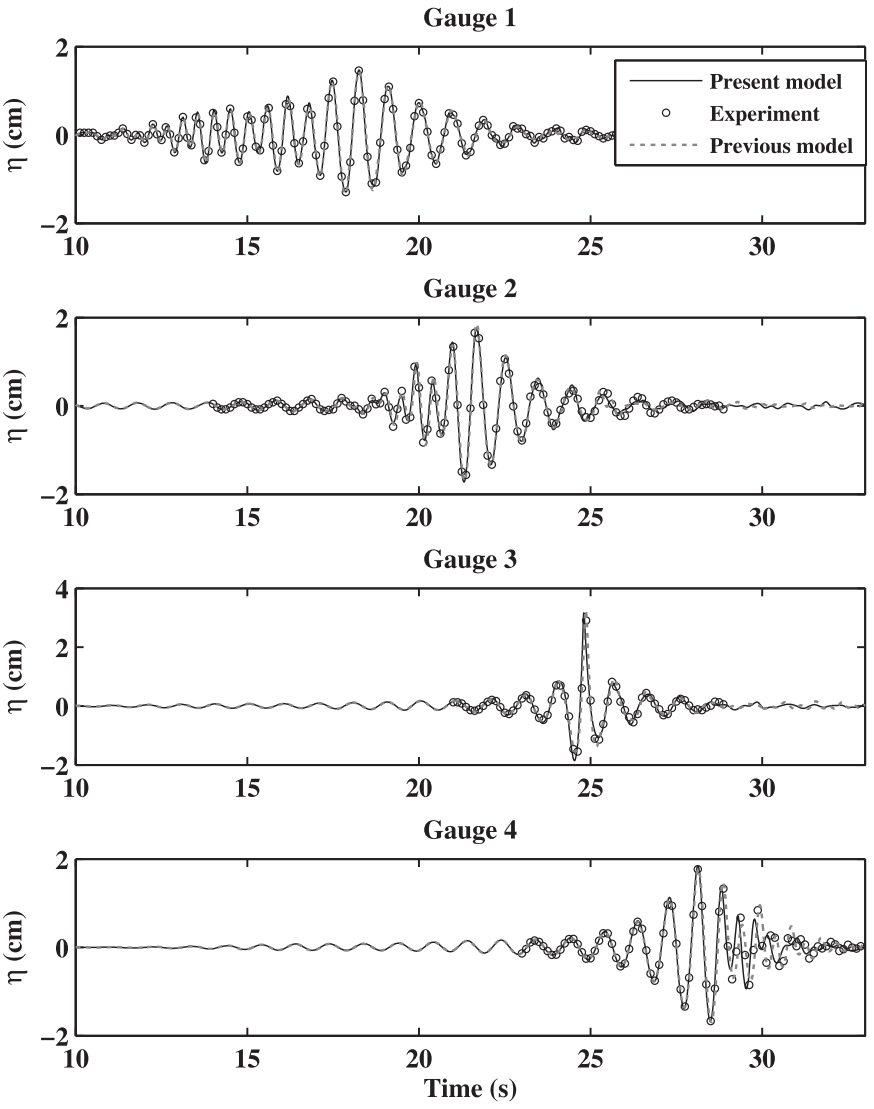

FIG. 2. The time evolution of surface elevations at the four wave gauge locations without wind. Solid line indicates the present model, circles indicate the experiment by Tian and Choi (2013), and the dotted line indicates the pseudospectral model by Tian and Choi (2013).

prediction by Tian and Choi (2013). These differences are largely due to different ways to account for wind forcing in these models. In the experiment no wind profile was measured at gauge G1, the inlet of the numerical wave tank. A uniform wind profile was applied in the present two-phase flow simulation. While in the pseudospectral wave model of Tian and Choi (2013), the wind forcing was applied through a surface pressure term combining Miles' shear flow instability theory (Miles 1957) and Jeffreys' sheltering hypothesis (Jeffreys 1925). Airflow separation was taken into account through a criterion proposed therein depending on the wind speed and local wave steepness in Tian and Choi (2013). The present two-phase flow model solves the air and water phases simultaneously and avoids these empirical parameterizations. In addition, the two-phase flow approach is able to capture both the air and water flow motion through a synoptic two-way coupling.

Despite the difference in wind forcing at the inlet, the comparisons are overall very good. To better evaluate the performance of the model, Fig. 4 shows a detailed comparison of surface elevations at gauges G3 and G4 under the largest wind speed of $U_0 = 5.0\,\mathrm{m\,s^{-1}}$. The present model prediction of the surface profile, especially the wave phase, is in better agreement with the experiment than the pseudospectral model.

Both models tend to overpredict the peak surface elevation at wave gauge G3 (cf. Figs. 3–4). This suggests

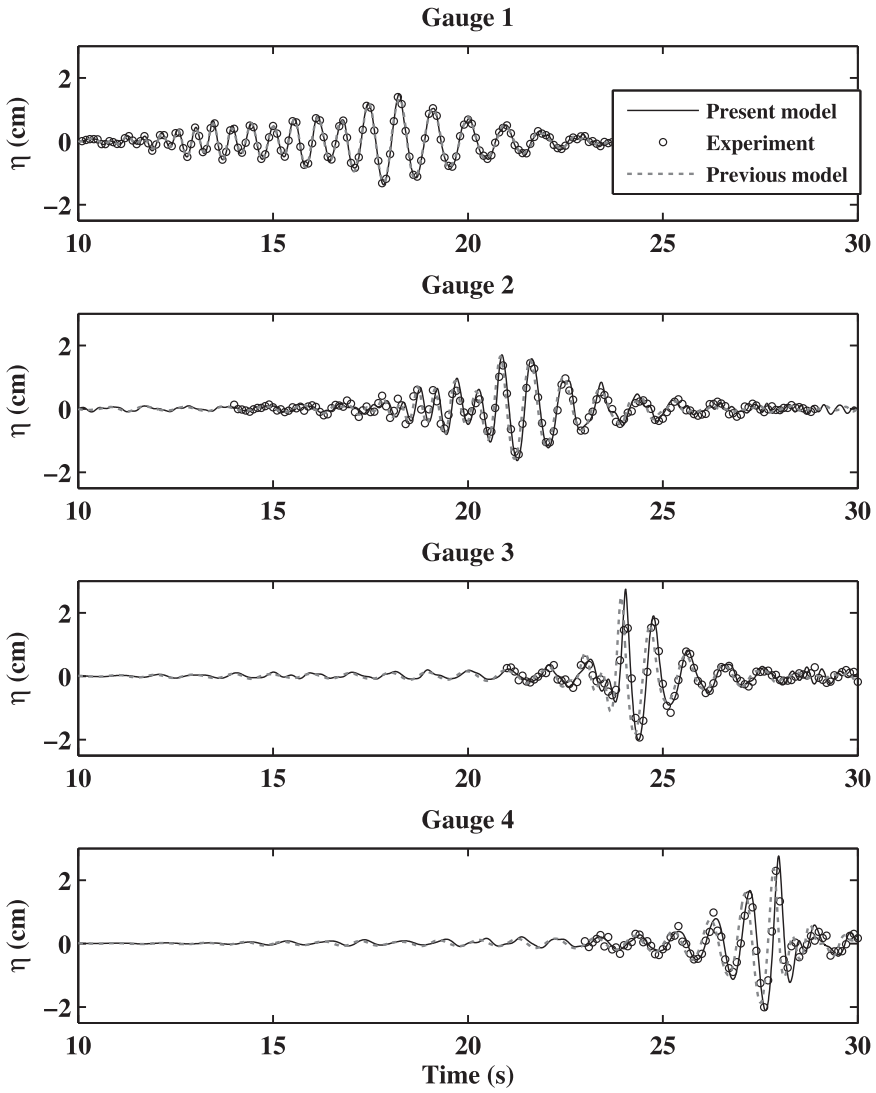

FIG. 3. As in Fig. 2, but for a following wind speed $U_0 = 3.2\,\mathrm{m\,s^{-1}}$.

that some source of dissipation inside the physical wave tank was not captured by either model. To account for the damping at the free surface and the frictional loss at the tank sidewalls and bottom, an equivalent kinematic viscosity $\nu = 5 \times 10^{-6}\,\mathrm{m^2\,s^{-1}}$ was used in Tian and Choi (2013). Microscale breaking waves, locally generated short wind waves that break without entraining air, may be another source of dissipation. They were observed in the previous laboratory studies at wind speeds as low as approximately $4\,\mathrm{m\,s^{-1}}$. Siddiqui and Loewen (2007) showed that the percentage of microscale breaking waves increased abruptly from 11% to 80% as the wind speed increased from 4.5 to $7.4\,\mathrm{m\,s^{-1}}$.

Apart from the direct wind forcing, the wind-driven current is another important factor for the wind effects on the evolution of wave groups. The presence of wind forcing introduces a thin surface drift current layer, which has high vorticity due to a strongly depth-dependent current profile (Phillips and Banner 1974). However, because of model ability limitation, in the past this layer has typically been modeled as a uniform current with a magnitude a few percent of the free stream wind speed, for example, the fully nonlinear potential flow model (Kharif et al. 2008; Yan and Ma 2011) and the pseudospectral model (Tian and Choi 2013). Tian and Choi (2013) tried three current speeds and found that the one equal to 0.9% of the free stream wind speed produced acceptable wave amplitudes, but there was a small phase shift between their model and the measurement (see Fig. 4).

It is evident, however, that a better prediction of the observed surface profile and wave phase was achieved

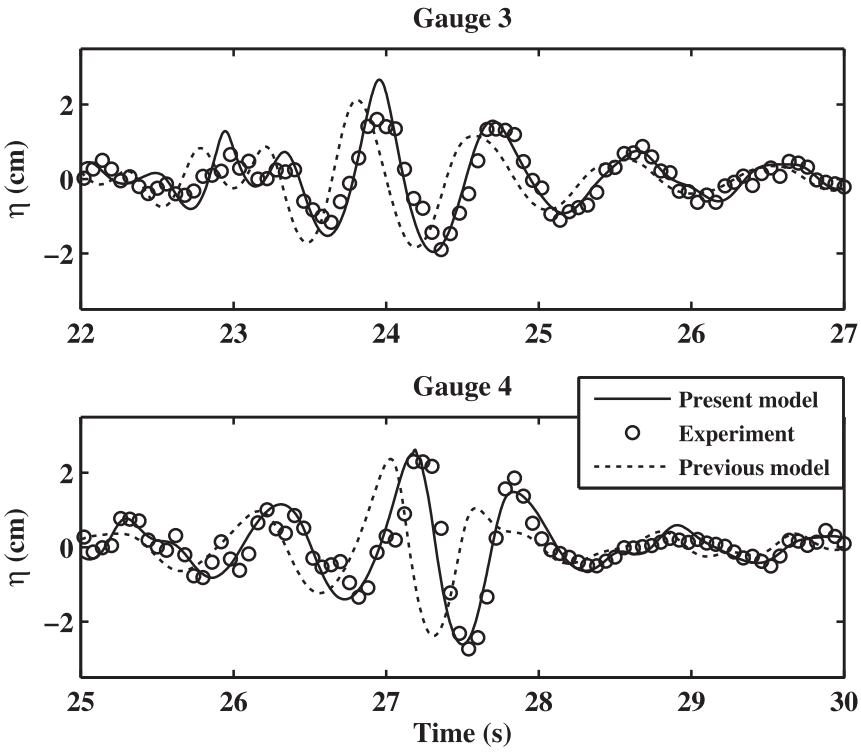

FIG. 4. The time evolution of wave surface elevations at gauge G3 and G4 locations under a following wind speed $U_0 = 5.0\,\mathrm{m\,s^{-1}}$. Solid line indicates the present model, circles indicate the experiment by Tian and Choi (2013), and the dotted line indicates the pseudospectral model by Tian and Choi (2013).

by the present model without artificially introducing a uniform current to account for the wind-driven current effect. Unlike the previous wind and wave models mentioned above, the present two-phase Navier–Stokes model solves the air and water flow simultaneously, and the surface current is generated naturally by the wind forcing through air and water coupling.

c. *Evolution of the wave group under following and opposing wind*

The effect of opposing wind on the evolution of the same focusing wave group is examined in this section. Figure 5a shows the comparison of spatial distribution of maximum surface elevations under zero wind, following ($U_0 = 5.0\,\mathrm{m\,s^{-1}}$), and opposing wind ($U_0 = -5.0\,\mathrm{m\,s^{-1}}$). It is evident from the figure that the focus point is shifted from $x = 7.1$ m under no wind downstream to $x = 8.7$ m under the following wind and upstream to $x = 6.1$ m under the opposing wind. The peak surface elevation at the focus point is increased/decreased by the following/opposing wind forcing. Figure 5b shows the corresponding time history of the surface elevations at the focus point for the following and opposing wind. In contrast to the following wind, the opposing wind accelerates the focusing process. The focus time is shifted from 25.0 s under no wind to 23.4 s under opposing wind $U_0 = -5.0\,\mathrm{m\,s^{-1}}$.

d. *Wind effect on wave focus point and amplification*

The spatial distribution of the maximum surface elevations and wave height of the wave group is examined in this section. Figure 6 shows the comparison of the present model results with the experimental data and the pseudospectral model predictions by Tian and Choi (2013). Two wind forcing conditions, $U_0 = 0$ and $5.0\,\mathrm{m\,s^{-1}}$, are used for which Tian and Choi's (2013) model results are available. It is evident from Fig. 6a that there is overall a good agreement between models and experiments for $U_0 = 0\,\mathrm{m\,s^{-1}}$. As shown in Fig. 6b, under a large wind forcing $U_0 = 5.0\,\mathrm{m\,s^{-1}}$, the focus point where the maximum surface elevation occurs is well predicted by both models, and it is shifted downstream from $x = 7.1$ m under no wind to $x = 8.7$ m under a strong wind $U_0 = 5.0\,\mathrm{m\,s^{-1}}$. The peak surface elevation at the focus point $x = 8.7$ m is well captured by the present model but severely underpredicted by Tian and Choi's model (cf. Fig. 6b).

Figure 7 shows the wind effects on the extreme wave surface elevation at the focus point and its spatial and temporal location. Figure 7a indicates that the extreme

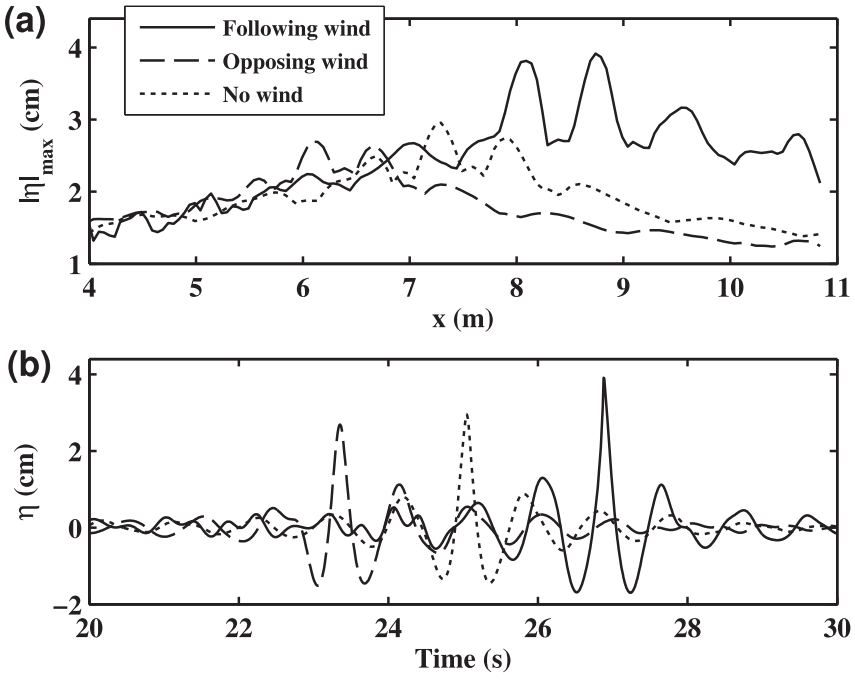

FIG. 5. (a) Spatial distribution of the maximum surface elevations of wave group and (b) time history of surface elevation at the focusing point under zero wind, following wind ($U_0 = 5.0\,\mathrm{m\,s^{-1}}$), and opposing wind ($U_0 = -5.0\,\mathrm{m\,s^{-1}}$).

wave surface elevation at the focus point decreases/increases with the following wind speed at weak/strong wind forcing. These results are consistent with the numerical results by Yan and Ma (2012) and are due to the two competing mechanisms: the direct wind forcing versus the wind-driven current. On one hand, the direct following wind forcing causes wave growth (Miles 1957). On the other hand, the presence of the following current induced by the wind leads to decreased wave height at the focus point (Ning et al. 2015). The direct wind forcing by a small wind speed $U_0 = 1.4\,\mathrm{m\,s^{-1}}$ has negligible effect on wave growth, while the wind-driven current modifies the wave dispersion and therefore nonoptimal focusing or defocusing of wave components, reducing the maximum wave height slightly. Under a large wind speed, for example, $U_0 = 5.0\,\mathrm{m\,s^{-1}}$, however, the strong direct wind forcing dominates over the defocusing effect due to the wind-driven current; therefore, the extreme wave height at the focus point increases with wind speed. Figures 7b and 7c show that as the following wind speed increases, the focus point is shifted increasingly downstream and occurs at a later time.

The effect of opposing wind on the extreme wave surface elevations at the focus point and its focusing location and time is also shown in Fig. 7. The extreme wave surface elevation at the focus point decreases with increasing opposing wind speeds. The shifts of the focusing point location and time have an opposite trend to those under following wind, and the shifts under opposing wind are slightly smaller than those under following wind (Figs. 7b,c). In contrast to the case of following wind, the wind-driven current by the opposing wind may increase the extreme wave height by shortening the wavelength or decrease it through nonoptimal focusing by altering the phase speeds of the wave components and may even block some components if the current is strong enough. It is seen in Fig. 7a, however, that the weak opposing wind $U_0 = -1.4\,\mathrm{m\,s^{-1}}$ reduces the extreme wave surface elevation at the focus point. It is likely that the shortening and steepening wave effect of opposing drift current may not be large enough to counteract the combined effects of nonoptimal focusing by the wind drift and opposing direct wind forcing.

To examine the wave height evolution along the flume under the following and opposing wind, we use the same amplification factor as Kharif et al. (2008), that is, $A = H_{\max}/H_{\mathrm{ref}}$, where $H_{\max}$ is the maximum wave height between two consecutive crests and troughs at each location, and H_{ref} is the maximum wave height at wave gauge G1 without wind action. The spatial variations of the amplification factor for the nonbreaking wave group (DF 1 in Table 1 of Tian and Choi 2013) are shown in Figs. 8a and 8c, and those for the breaking counterpart

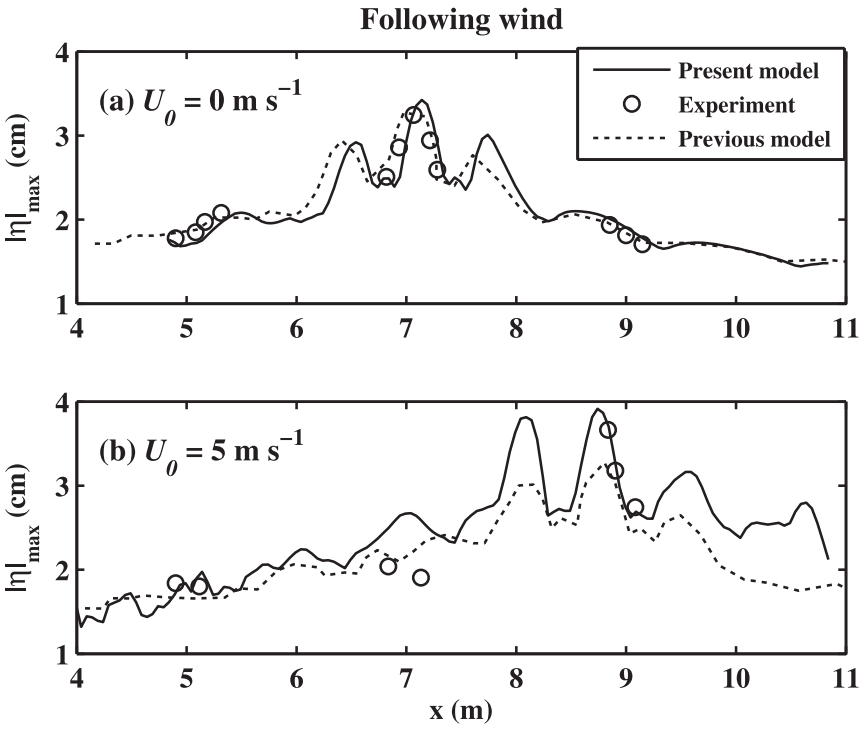

FIG. 6. Comparison of maximum surface elevations as a function of distance from the physical test wavemaker for wind speeds: (a) $U_0 = 0\,\mathrm{m\,s^{-1}}$ and (b) $U_0 = 5.0\,\mathrm{m\,s^{-1}}$. Solid line indicates the present model, circles indicate the experiment by Tian and Choi (2013), and the dotted line indicates the pseudospectral model by Tian and Choi (2013).

(DF 2 in Table 1 of Tian and Choi 2013) are shown in Figs. 8b and 8d.

For the nonbreaking wave group, it is noted that the presence of following wind leads to an asymmetry in the wave amplification and deamplification during the focusing and defocusing stages before and after the focus point (Fig. 8a). This behavior is more pronounced than the evolution of peak surface elevation shown in Fig. 6b. In the absence of wind, the rate of change of the extreme wave height of the group is symmetric relative to the focus point. In the presence of following wind, the rate of change of wave height at the defocusing stage is smaller than that at the focusing stage. The extreme wave height is increased significantly by the following wind action during the defocusing stage. This slower defocusing process, shift of focus point, and increases of extreme wave height will increase the life-span of the freak wave event, since the freak wave criterion $A > 2$–2.2 (Kharif and Pelinovsky 2003) is satisfied for a longer period of time. Similar asymmetric behavior has been observed in experimental studies by Touboul et al. (2006) and Kharif et al. (2008). This asymmetric behavior, however, was not captured by the pseudospectral model by Tian and Choi (2013) as shown in their Fig. 15.

In the presence of opposing wind, unlike the case of following wind, the rate of change of maximum wave height at the focusing and defocusing stage is more or less the same (Fig. 8c). The rate of change is larger than that without wind or with following wind during the focusing stage. This in combination with the reduced peak wave height shortens the duration of the extreme wave event.

The wind effect on the amplification factor for the large breaking wave group is not as obvious. There are more variations of wave height during the focusing stage. The amplification factor is overall smaller than that for the nonbreaking group, since the breaking wave group has a larger wave height at the wavemaker and the steepness-limited wave breaking prevents further increase of the wave height. In the absence of wind, a plunging breaker occurs at $x = 6.3$ m, in comparison with the focus point $x = 7.1$ m of the nonbreaking wave group (see also Fig. 6a). In the presence of following wind, the breaking location is shifted slightly downstream, and the incipient breaking wave height increases with the following wind speed. In the presence of opposing wind, the breaking location is shifted slightly upstream, and the peak wave height may become larger and then smaller, depending on the

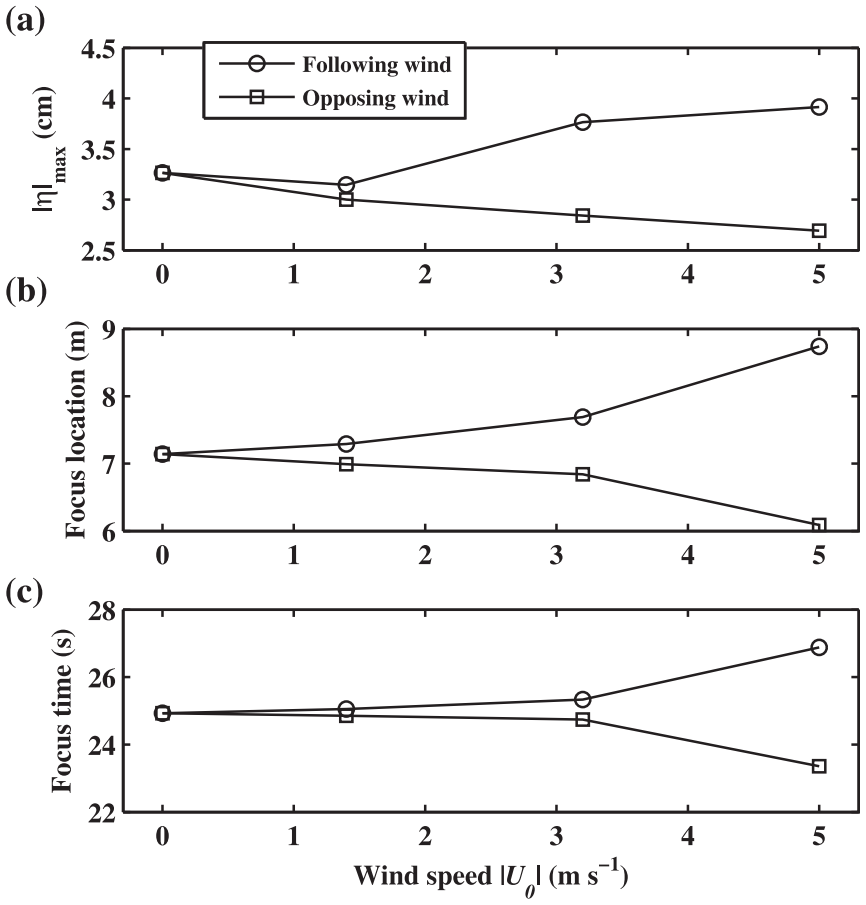

FIG. 7. (a) Maximum surface elevations of focus wave group at focus point, (b) wave focusing location, and (c) time as a function of wind speeds for following and opposing wind.

relative importance of the opposing drift current and direct wind forcing. Strong opposing wind may even prevent the breaking from occurring. More details about the wind effect on breaking are described in section 5c on airflow structure.

5. Mechanisms of wind effect on wave group

a. Wind-driven current effect

As discussed in the introduction, the wind affects the evolution of a focusing wave group through the direct wind forcing and wind-driven current. In this section, the separate effect of wind-driven current and its vertical shear is examined. Following Tian and Choi (2013), a uniform current speed equal to 0.9% of U_0 ($0.009U_0$) is used in the present model. The sole effect of the uniform current on the evolution of a wave group is examined.

The wind-driven current typically exists only within a thin layer below the water surface. It varies with depth and depends on the measurement locations, that is, fetch, wave trough, or crest (Peirson and Banner 2003; Longo et al. 2012). We assume a thin surface layer current and examine its effect on the wave group evolution. An exponential current profile approximates well the predicted current profile by the present two-phase flow model (squares in Fig. 9) and resembles the observed surface wind drift layer (Tsuruya et al. 1985; Savelyev et al. 2011; Longo et al. 2012). The exponentially sheared layer current is given by

$$U_c(z) = U_s \exp(z/\delta), \quad -d < z < \eta, \tag{11}$$

where U_s is the surface current velocity, and δ is a characteristic current layer thickness with the current decaying to 4% of its surface value at $z = -\pi\delta$. The same vertical current profile has been used by Nwogu (2009) to examine the modulational instability of gravity waves in a sheared current. When approximating the dispersion relation for waves on a weak

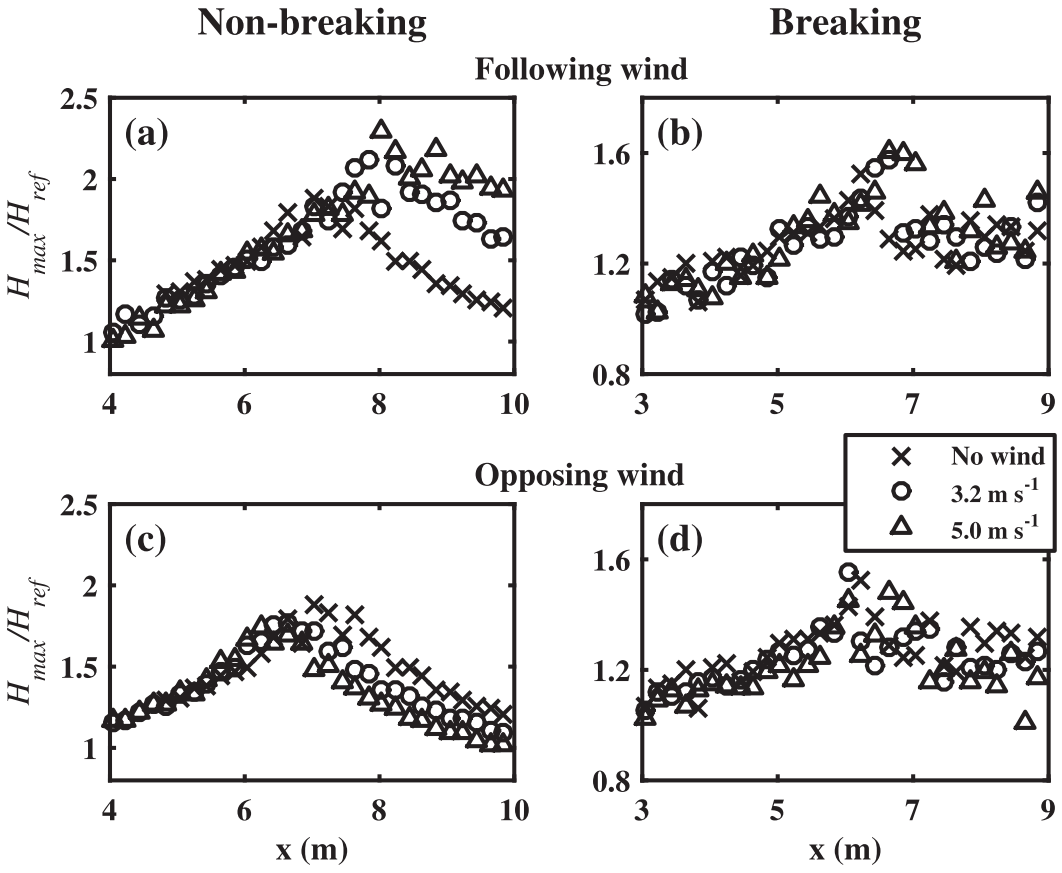

FIG. 8. Spatial distribution of wave amplification factors for (a),(c) a small nonbreaking wave group (DF 1 in Table 1 of Tian and Choi 2013) and (b),(d) a large breaking wave group (DF 2 in Table 1 of Tian and Choi 2013). (top) Following wind. (bottom) Opposing wind.

current, Kirby and Chen (1989) also considered a linearly sheared surface layer current:

$$U_c(z) = U_s(1 + z/\Delta), \quad -\Delta < z < \eta, \tag{12}$$

where Δ is the layer thickness within which the linearly sheared layer current decreases from its surface value to zero. Both exponential and linear current profiles have the same current velocity and shear at the free surface when $\Delta = \delta$. The two current profiles have the same mass flux when $\Delta = 2\delta$. The surface current velocity is related to the friction velocity u^* of the airflow by (Wu 1975) $U_s = 0.55\ u^* = 0.12\,\mathrm{m\,s^{-1}}$, where the measured mean friction velocity u^* in Table 2 of Tian and Choi (2013) is used.

Figure 10a compares the uniform current and wind forcing effect on the spatial distribution of maximum surface elevations under a following wind speed $U_0 = 5.0\,\mathrm{m\,s^{-1}}$. In the pseudospectral model prediction by Tian and Choi (2013), both the wind-driven current and direct wind forcing were considered. The main difference between the wave–current interaction simulation by the present model and Tian and Choi's (2013) prediction is that wind forcing was incorporated in the latter by combining Miles' and Jeffreys' sheltering model for direct wind forcing and by including a uniform wind-driven current.

As seen in Fig. 10a, the predicted maximum surface elevations by the present model (solid line) without wind but with wind drift current differ significantly from those by Tian and Choi's (2013) pseudospectral wave model with wind forcing (dashed line). The wind forcing modeling in the pseudospectral model is responsible for this difference. The present model considering only the uniform wind drift current underpredicts the observed wave elevations, and it shifts the focus point downstream as observed. This indicates that the uniform wind-driven current plays a dominant role in shifting the focus point downstream, while the direct wind forcing is responsible for the observed wave height increase.

Figure 10b shows the effect of a thin surface layer current on the evolution of the wave group. The current

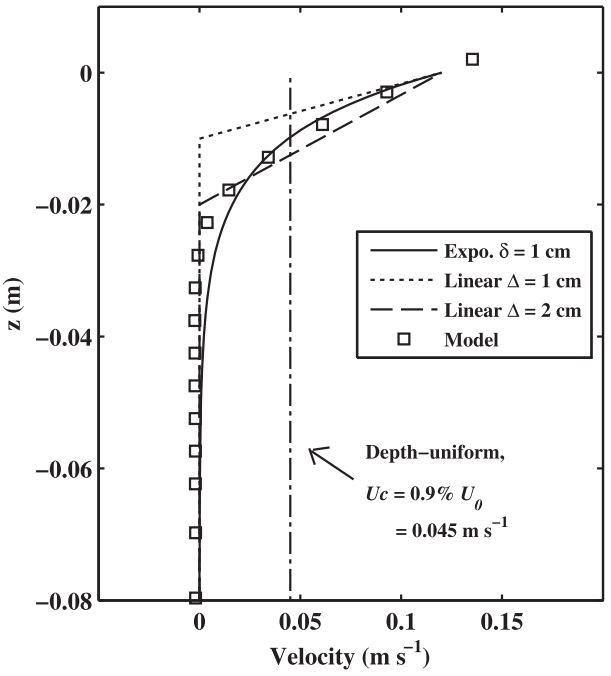

FIG. 9. Surface layer wind drift current profiles with an exponential shear (solid line; the surface velocity is reduced by 96% at the depth $z = -\pi\delta$) and linear shear (dashed line and dotted line; Δ is the layer thickness over which the wind drift velocity decays to zero) to replicate the observed wind drift current profiles such as those in Longo et al. (2012). Squares indicate the predicted wind drift profile by the present model at wave gauge G2.

profiles have the same surface velocity $U_s = 0.12\,\mathrm{m\,s^{-1}}$. The vertical shear of the current has an important effect on the spatial distribution of the maximum surface elevations. For simplicity, the result for the linear shear current with $\Delta = 1\,\mathrm{cm}$ is not included in Fig. 10b. We observed that the exponential profile shifts the focus point more downstream than the linear profile with $\Delta = \delta = 1\,\mathrm{cm}$, although both profiles have the same surface velocity and current shear. For current profiles with the same mass flux $\Delta = 2\delta = 2\,\mathrm{cm}$, the wave group evolves similarly before approaching the focus point. But as a result of the accumulation effect, a slight difference appears when the wave components start to collapse at the focus point. The dimensionless parameter $k\Delta$ or $k\delta$, where k is the wavenumber for the primary wave component, may be used to quantify the current effect on the shift of the focus point.

Figure 11 shows the time evolution of surface elevations at gauge G3 and G4 locations in the presence of uniform current ($U_c = 0.045\,\mathrm{m\,s^{-1}}$), and linearly and exponentially sheared currents ($U_s = 0.12\,\mathrm{m\,s^{-1}}$) in a thin surface layer as indicated in Fig. 9. The focus point is shifted in time when the current is adopted in the model simulation to represent the wind-driven current. However, the prediction of the focusing time is improved when the surface layer currents with exponential and linear shear are used instead of uniform current. It is worth noticing that all three current profiles are capable of reproducing the spatial shift of the focus point induced by the wind-driven current (see Fig. 10).

Figure 12a compares the spatial distributions of maximum surface elevations of the focusing wave group under four combinations of surface layer current and following wind forcing $U_0 = 5.0\,\mathrm{m\,s^{-1}}$. It is seen that the exponentially sheared surface layer current with $\delta = 1\,\mathrm{cm}$ shifts the focus point downstream as far as wind forcing only. It should be noted that the current is only applied to a thin layer of 0.04 m beneath the surface, as opposed to the entire water depth of 0.54 m for the uniform current profile used in Fig. 10a. The exponentially sheared surface layer current is therefore expected to induce less modulation to the wave group's evolution than the depth-uniform current. We noticed that the presence of uniform current in Fig. 10a decreases considerably the surface elevation at the focus point, while the presence of an exponentially sheared current in Fig. 12a results in virtually no decrease on the surface elevation. The maximum surface elevation at the focus point even increases slightly under the linearly sheared current in Fig. 10b. These indicate that besides the direct wind forcing, the vertical current shear also plays an important role in modulating the evolution of a wave group. The present model results are consistent with those of Banner and Song (2002) in that the presence of a surface shear would destabilize the wave group and thus may lead to wave breaking if the current shear strength and wave steepness are large enough.

The exponentially sheared surface layer current is a good approximation of the wind-driven current profile (see Fig. 9) and is added as an external forcing to the model in addition to the wind forcing and the wind-driven current. Figure 12a further demonstrates the current influence on the evolution of the wave group in the presence of wind. The comparison of the wind + current result (dashed line) with that of wind only (dotted line) indicates that adding the surface layer current shifts the focus point farther downstream from $x = 8.7$ to 10.4 m and increases the maximum surface elevation. The downstream shift of the focus point makes it possible for the wave to experience a longer duration of wind forcing and thus to focus with a larger wave height. The asymmetry of maximum surface elevations between the focusing and defocusing stages still exists, as in the cases of the wind forcing only (Touboul et al. 2006; Kharif et al. 2008).

The separate effect of opposing wind drift current on the evolution of the wave group is examined in the same

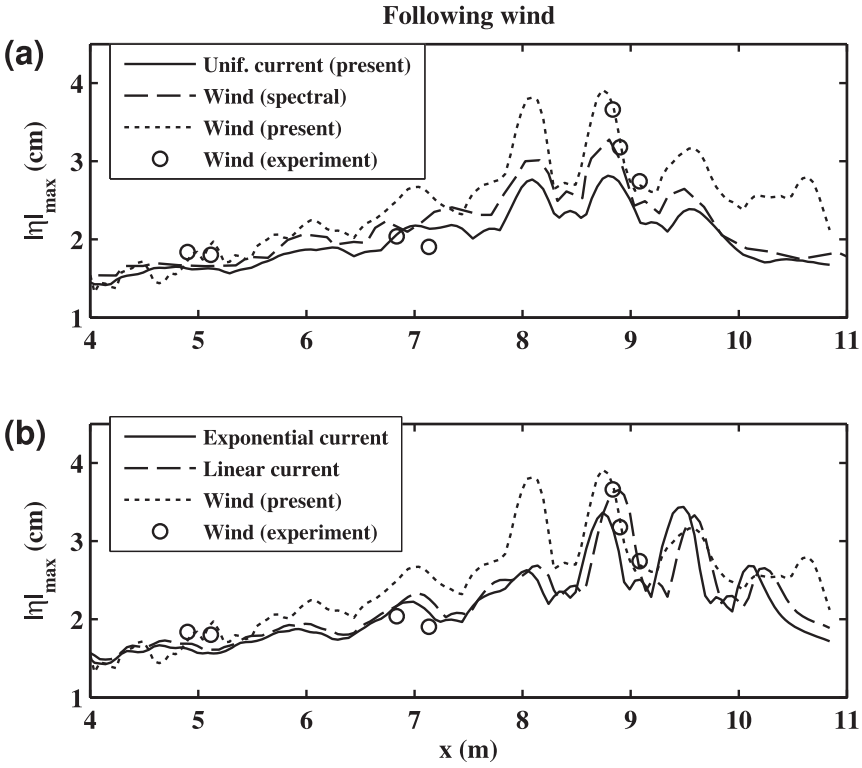

FIG. 10. Comparison of the effect of current with and without vertical shear and wind forcing on the spatial distribution of maximum surface elevations under following wind speed $U_0 = 5.0\,\mathrm{m\,s^{-1}}$. Dotted line indicates the present model prediction with wave + wind and circles indicate the experiment with wave + wind (Tian and Choi 2013). (a) Uniform current ($U_c = 0.009U_0$). Solid line indicates the present model with wave + uniform current, and dashed line indicates the pseudospectral model with both uniform current and direct wind forcing by Tian and Choi (2013). (b) Surface layer current (see Fig. 9). Solid line indicates the present model with wave + exponential current (current layer thickness $\delta = 1\,\mathrm{cm}$), and dashed line indicates the present model with wave + linear current (current layer thickness $\Delta = 2\,\mathrm{cm}$).

manner as the following wind. Both the depth-uniform ($U_c = 0.009U_0$) and exponentially sheared surface layer current ($\delta = 1\,\mathrm{cm}$) are used. For simplicity, the result for the uniform current is not included in Fig. 12b. We observed that the uniform opposing current leads to significantly larger surface elevation than the exponentially sheared surface layer current. While both current profiles shift the focus point upstream, the predicted focus point location and peak surface elevation by the surface layer current with exponential shear (solid line) are in a better agreement with the wind forcing only results. The comparison of the wind + current result (dashed line) with that of wind only (dotted line) indicates that adding the surface layer current shifts the focus point farther upstream from $x = 6.09$ to $5.64\,\mathrm{m}$.

b. *Airflow structure above extreme waves*

The dynamics of airflow structure over surface waves plays an important role in the momentum, mass, and energy transfer across the air–sea interface. We have presented so far the wind effect on a nonbreaking dispersive focusing wave group; however, our findings about the role of the surface layer current in wind effect apply to the breaking wave group DF 2 (Zou and Chen 2016). A plunging breaker was observed for this dispersive focusing group in the absence of wind. The major characteristics of wave breaking events, namely, overturning jet, plunging, air entrainment, splash-up, and vertical jet, are well captured by the two-phase flow model in Fig. 13. We ran the present two-phase flow model for breaking wave group DF 2 for both following and opposing wind with various magnitudes (cf. Fig. 8). According to the spatial evolution of wave profiles under these wind conditions, we found that the following wind delays the breaking and shifts the breaking location downstream, whereas the opposing wind slightly accelerates the breaking and shifts the breaking location upstream. The wind-induced drift current is mainly responsible for these shifts of the breaking time and location. However, with increasing wind speeds, the wind

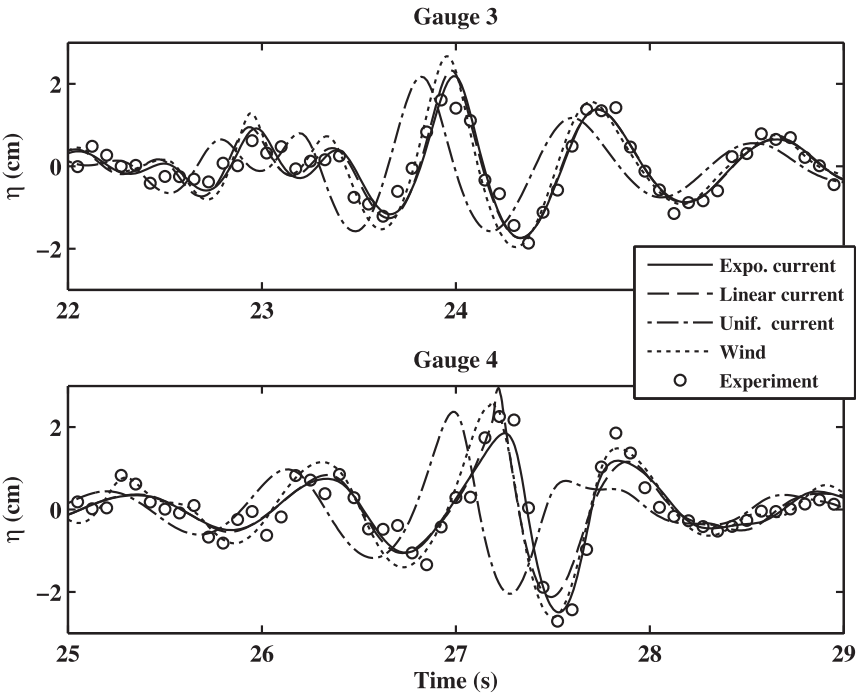

FIG. 11. The effects of depth-uniform current (current velocity $U_c = 0.009U_0$; dashed–dotted line), linearly (current layer thickness $\Delta = 2$ cm; dashed line), and exponentially (current layer thickness $\delta = 1$ cm; solid line) sheared current (surface current $U_s = 0.12\,\mathrm{m\,s^{-1}}$) in a thin layer on the time history of surface elevations at G3 and G4. Dotted line indicates the present model for following wind $U_0 = 5.0\,\mathrm{m\,s^{-1}}$.

forcing starts to play an increasingly larger role in affecting the wave breaking so that the wind effect on breaking is in contrast to what is described above. The strong following wind may enhance wave breaking, while the opposing wind may be strong enough to prevent the plunging breaker from occurring.

In this section, airflow structure above the breaking wave group in Tian and Choi (2013) is examined. The airflow structure above the nonbreaking wave group exhibits similar but less pronounced features.

Figure 13 show the velocity and vorticity fields of the instantaneous airflow structure above the extreme waves, without wind and with following wind $U_0 = 3.2\,\mathrm{m\,s^{-1}}$ and opposing wind $U_0 = -3.2\,\mathrm{m\,s^{-1}}$. Note the scale range of the vorticity and velocity vector is different for these three wind forcings in Fig. 13. The magnitude of vorticity for the opposing wind is much more pronounced than that for the following wind. This is due to the larger relative wind speed to the propagating wave in the opposite direction and the blunt-shaped wave front face under the opposing wind.

In the absence of wind (Figs. 13a–d), the airflow is driven by the wave propagation and surface profile changes. A counterclockwise recirculation of airflow is formed above the wave crest and travels with the wave. As the front face of the crest curls forward and the plunging jet is about to impinge on the water surface ahead, large velocities appear beneath the overturning jet, since the air tries to escape from the enclosing cavity through a narrow gap. The jet impact on the surface causes a significant splash-up and a second plunge, which is amplified farther downstream. There is a layer of positive vorticity (red) in the air due to the recirculating airflow above the crest, and a thin layer of negative vorticity beneath the plunging jet and above the wave trough in front of the breaker. The negative vorticity in the water appears first in the front face of the crest, and then spreads around the curling plunger where the surface topology changes drastically. The magnitude of vorticity in the water is overall smaller than that in the air.

In the presence of the following wind (Figs. 13e–h), because of large velocity difference across the air–water interface, a shear layer of airflow with strong negative vorticity (blue) is attached above the rear face of the breaking wave and separates from the air–water interface at a point where there is an abrupt change in the free-surface slope. The free shear layer developed downwind of the separation point is sufficiently thin and moves high above the water surface, similar to what was observed in Reul et al. (2008). It remains coherent for some distance

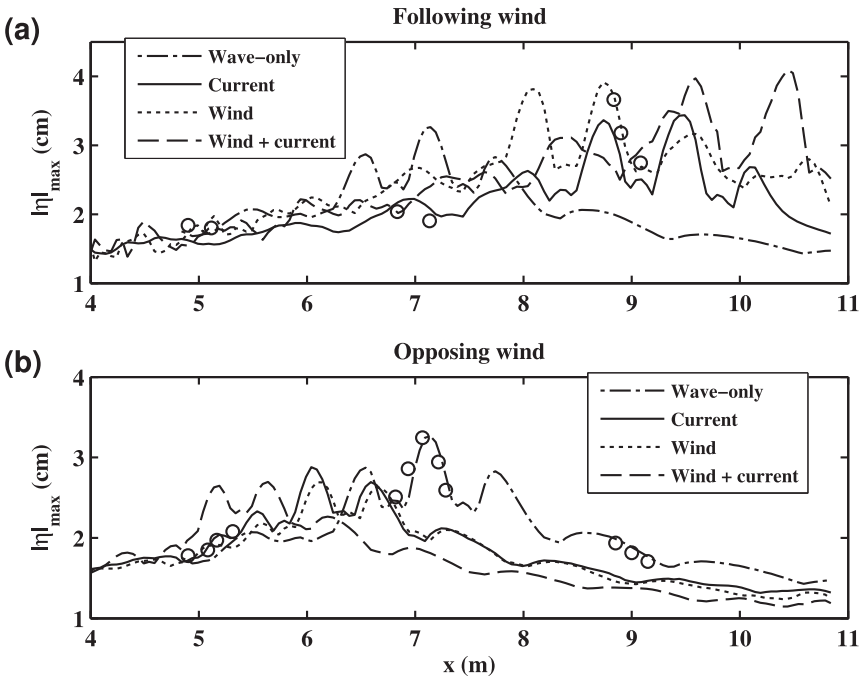

FIG. 12. Effect of the exponentially sheared (with layer thickness $\delta = 1$ cm) surface layer current on the maximum surface elevation of focus wave group for (a) following wind $U_0 = 5.0\,\mathrm{m\,s^{-1}}$ and (b) opposing wind $U_0 = -5.0\,\mathrm{m\,s^{-1}}$. Dashed–dotted line indicates wave only, solid line indicates wave + exponential shear current (wind-driven current), dotted line indicates wave + wind, dashed line indicates wave + wind + exponential shear current (external current), and circles in (a) indicate the experiment with following wind and circles in (b) indicate the experiment without wind by Tian and Choi (2013).

and then disintegrates into vortices, similar to the airflow observed above wind-wave crests shown in Fig. 6c1 of Buckley and Veron (2016). The airflow structure is similar to that over a backward-facing step beneath a following wind. In the immediate vicinity shadowed by the crest front, however, the airflow is at least partly driven by the wave propagation and profile changes. This is demonstrated by the positive vorticity (red) in front of the plunging jet, which is present in the absence of wind (Figs. 13a–d). A strong, clockwise-rotating vortex (blue) is formed farther downwind after the first plunging breaking, resembling the flow structure of a separation bubble, and it was propelled by the separation flow to a much higher position than those for the opposing wind (third column in Fig. 13). It is noted that the separated layer after the breaking wave crest does not reattach at the windward face of the preceding wave crest, where the presence of a vortex prohibits it from happening. The actual reattachment point is farther downwind, where the vortex has been convected away from the windward face of the preceding crest and the breaking wave crest becomes comparable with the growing preceding wave crest in size. This result implies the significant shadow effect on the preceding wave by the rogue wave.

In the presence of opposing wind (Figs. 13i–l), a shear layer of positive vorticity appears above the wave crest and its rear face due to the recirculating airflow downwind from the crest, same as that in the absence of wind. Because of the blunt-shaped front face of the wave crest, the shear layer separates from the rear face immediately after the apex of the crest and disintegrates into several counterclockwise-rotating vortices (red). This flow feature is similar to that over an airfoil at high angles of attack. These vortices then interact with the right-moving free surface below, leading to the formation of vorticity of opposite sign along the rear face of the wave. This phenomenon of primary vortices interacting with the free surface and the subsequent generation of secondary vortices has been observed experimentally by Techet and McDonald (2005) and numerically by Iafrati et al. (2013) in the absence of wind. The positive vortices expand and are advected downwind along the surface and interact with the incoming following wave crests propagating against the wind and gradually lose their strength (see Fig. 14).

By the comparisons of the evolution of breaking wave profiles with different wind forcing in Fig. 13, we may draw the conclusion that the breaking location is shifted

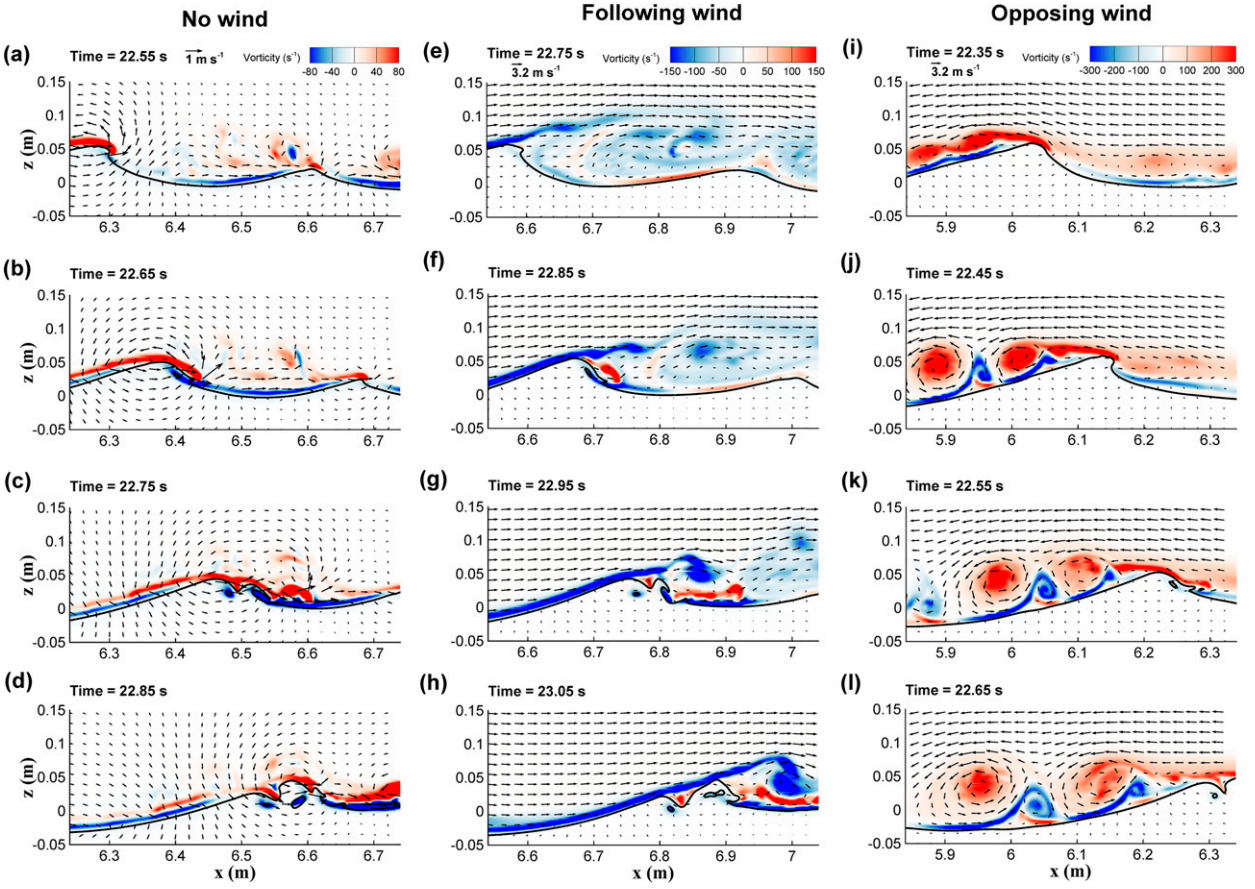

FIG. 13. Instantaneous velocity field (arrows) and vorticity (color) of airflow structure and wave profile (solid line) above a dispersive focusing, plunging breaking wave group (DF2 in Table 1 of Tian and Choi 2013). (a)–(d) No wind. (e)–(h) Following wind $U_0 = 3.2\ \mathrm{m\ s^{-1}}$. (i)–(l) Opposing wind $U_0 = -3.2\ \mathrm{m\ s^{-1}}$. Each column represents the time evolution of the wave profile and flow field and vorticity with a time interval of 0.1 s. Note the different scales of color bar for vorticity in each column.

downstream and the breaking is intensified with enlarged plunging tongue and breaker height by the following wind. In contrast, the breaking location is shifted upstream, and the breaking strength is suppressed by the opposing wind.

c. *Airflow separation effect on pressure and momentum fluxes*

Figure 15 shows the instantaneous pressure contours corresponding to the airflow structures shown in Fig. 13. The wind pressure distribution above the breaking wave crest is largely in accordance with the crest geometry and the vorticity distribution of the airflow. In the absence of wind (Figs. 15a–d), the minimum and maximum pressure appears above the crest and trough, roughly consistent with the potential flow theory. In the presence of following wind (Figs. 15e–h), a pressure depression appears at the core of the clockwise vortex (blue) on the downwind side of the wave crest. In the presence of opposing wind (Figs. 15i–l), high pressure appears at the windward side of the crest and low pressure appears above the crest. Two large pressure depressions are observed at the leeward side of the crest, corresponding to the two counterclockwise-rotating vortices (red) in Figs. 13i–l.

We placed pressure probes about 1 cm above the maximum wave crests following Kharif et al. (2008) and Reul et al. (2008) and calculated the form drag $p'\partial\eta/\partial x$ and the energy flux $-p'\partial\eta/\partial t$ from wind to waves. Figure 16 illustrates the instantaneous surface elevation, form drag, and energy flux for the cases presented in Figs. 13–14. The specific locations of the pressure probes are marked as squares in Fig. 15. Figure 16 indicates that the presence of extreme waves enhances the momentum and energy fluxes drastically (Figs. 16c–f), as demonstrated experimentally by Kharif et al. (2008). The airflow separation causes pressure drops in the leeward side of the crest and hence strongly affects the wind pressure–wave slope correlation as suggested by the experiment in Reul et al. (2008). While the following wind transfers momentum to the waves through a

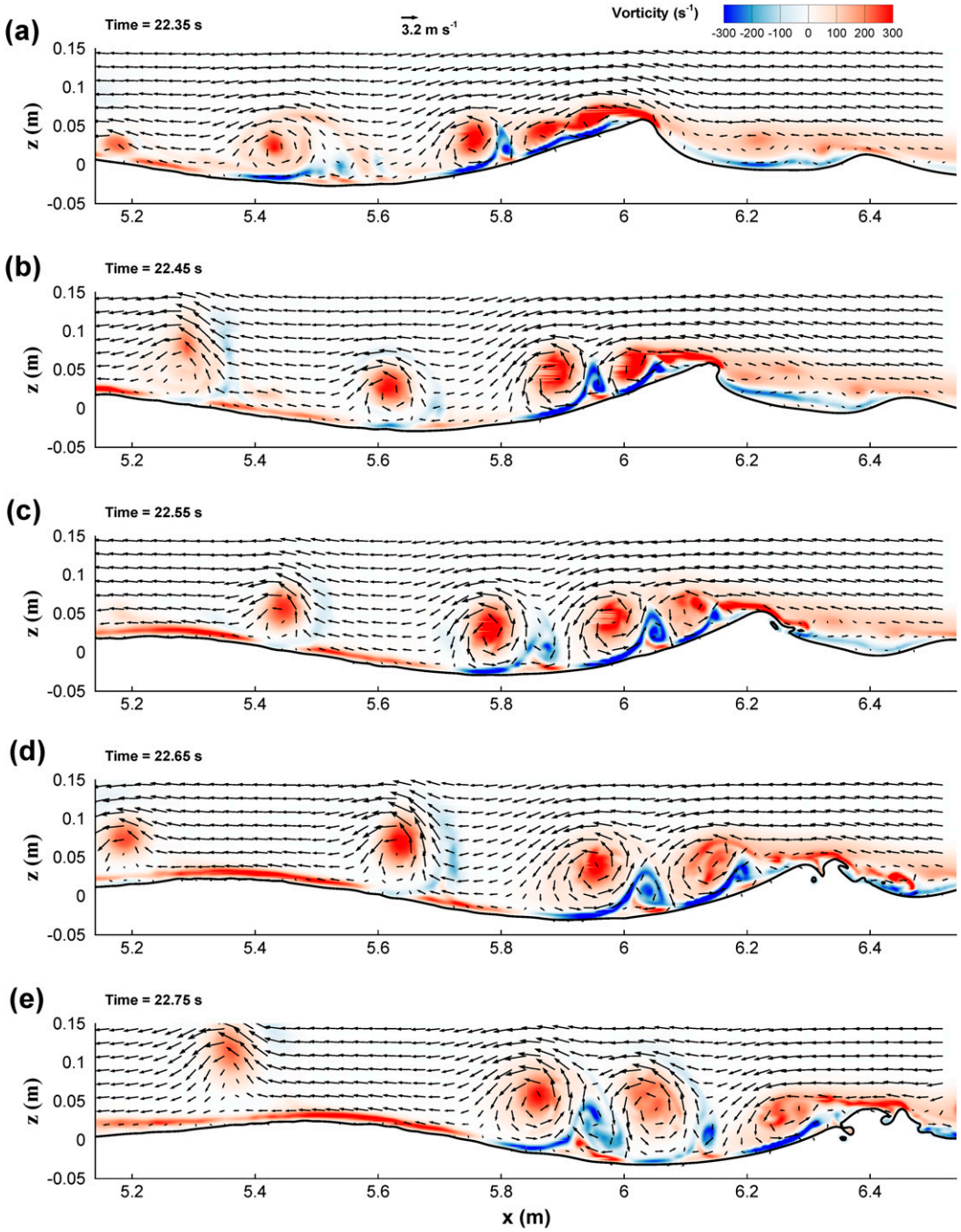

FIG. 14. Time evolution of the wave profile and flow field (arrows) and vorticity (color) with a time interval of 0.1 s above a dispersive focusing, plunging breaking wave group (DF2 in Table 1 of Tian and Choi 2013) in the presence of opposing wind $U_0 = -3.2\,\mathrm{m\,s^{-1}}$.

positive form drag (Fig. 16c), the opposing wind extracts the momentum from the waves through a negative form drag (Fig. 16d). The negative form drag persists over a noticeably long duration, which eventually would attenuate the waves. We noticed that the pressure drop in the presence of following wind is not as pronounced as that in the opposing wind since the vorticity in the latter is nearly twice as much as that for the following wind. The pressure–slope correlation curve for the following wind (Fig. 16c) has high and narrow peaks, similar to what was observed by Reul et al. (2008, see their Fig. 15b).

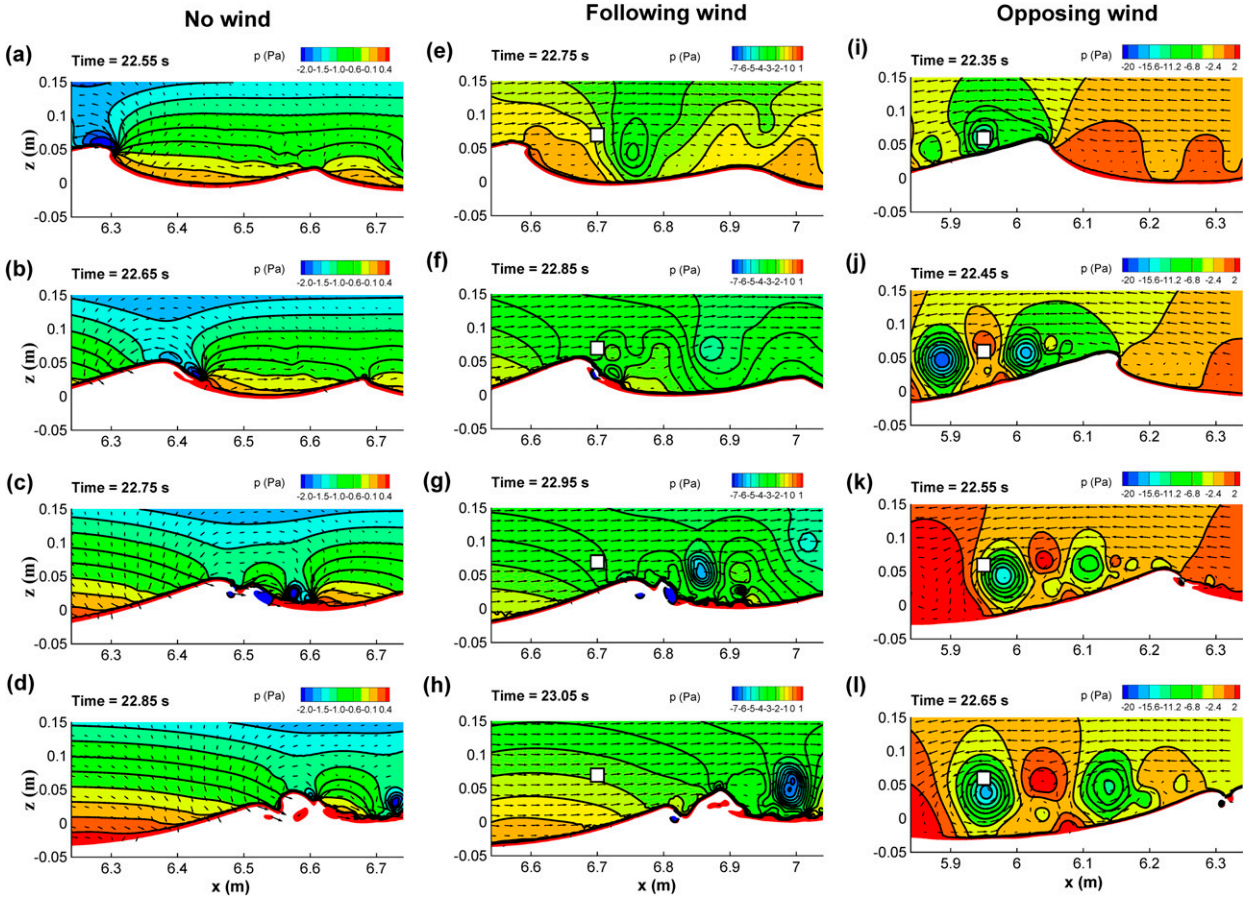

FIG. 15. Time evolution of wind pressure (color and black lines) and flow field (arrows) corresponding to the airflow structure shown in Fig. 13 with a time interval of 0.1 s. (a)–(d) No wind. (e)–(h) Following wind $U_0 = 3.2\,\mathrm{m\,s^{-1}}$. (i)–(l) Opposing wind $U_0 = -3.2\,\mathrm{m\,s^{-1}}$. Arrows indicate the same velocity field as in Fig. 13. White squares indicate the pressure probes used in Fig. 16.

While the wind-induced drift current is dominant in shifting the focus point, the direct wind forcing, which serves to amplify or damp the wave height through form drag, may modify the wave propagation speed through amplitude dispersion and thus indirectly shift the focus point. However, this effect would be conceivably small compared to the wind drift current effect.

6. Conclusions and discussion

The wind and current effects on the evolution of a breaking and nonbreaking dispersive focusing wave group are investigated numerically using a two-phase flow model. The turbulence is incorporated by the Smagorinsky subgrid-scale stress model, and the air–water interface is captured by the VOF method. As the air and water flow are solved simultaneously, the wind influences are incorporated through a synoptical, dynamical coupling of air and water instead of empirical parameterization. The predictions are in good agreement with the experiment without wind and with following wind. The effects of opposing wind and the strongly sheared surface layer current on the wave group's evolution are then examined. The separate contribution of direct wind forcing and wind-induced drift current and current shear is examined. The airflow structure above the extreme waves is investigated and linked with the energy flux between wind and wave.

It was found that the following wind-induced current shifts the focus point downstream and delays the wave group's focusing process. The shifts of focusing point in time and space increase with wind speed. Furthermore, the following wind with appreciable magnitude leads to a weak increase of the extreme wave height at the focus point and an asymmetry in the wave amplification and deamplification between the focusing and defocusing processes, consistent with experimental and numerical results by Touboul et al. (2006) and Kharif et al. (2008). In contrary, the wave amplification and deamplification is nearly symmetric relative to the focus point,

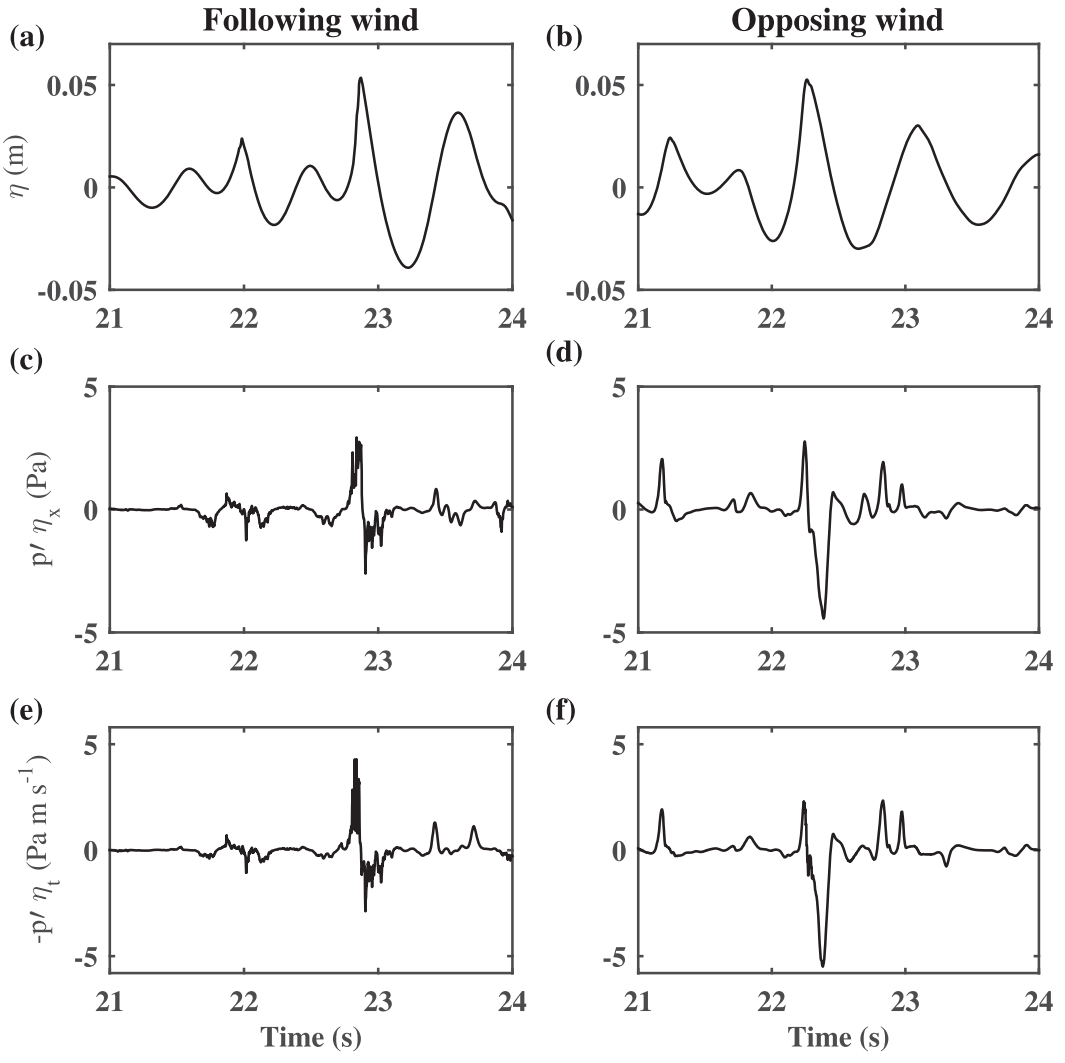

FIG. 16. Time history of (a),(b) surface elevation, (c),(d) form drag $p'\partial\eta/\partial x$, and (e),(f) energy flux from wind to waves $-p'\partial\eta/\partial t$ at 1 cm above the maximum crest for (left) following wind and (right) opposing wind (the pressure probes are marked as the white squares in Fig. 15). The symbol p' indicates the instantaneous perturbation pressure by wave action.

and the peak wave height and duration of the extreme wave event is reduced in the presence of opposing wind.

In the presence of weak following wind, the maximum surface elevation at the focus point decreases with increasing wind speed due to the dominance of the wind-driven current effect over direct wind forcing. The opposite is true for the strong following wind. Contrary to the case of following wind, our results show that the opposing wind shifts the focus point upstream and accelerates the focusing process of the wave group.

The present study demonstrates the importance of vertical variation of wind-driven current in the evolution of a dispersive focusing wave group. Our model results show that the thin surface layer current with a linear and exponential shear reproduces the observed and mode-predicted shift of the focus point by the wind forcing better than the depth-uniform current, for opposing wind in particular. The depth-uniform current leads to a significantly underpredicted surface elevation for following wind, and overpredicted surface elevation for opposing wind, while the thin surface layer current leads to reasonable surface elevation predictions for both cases. This result suggests that the depth-uniform current is not a proper representation of the wind-driven current effect in wind influences on focused wave groups. Although all the current profiles reproduce the spatial shift of the focus point under wind forcing, we found that only the thin surface layer current with vertical shear gives

overall better prediction of the observed temporal evolution of wave group. As noted by Nwogu (2009), the correct representation of the near-surface current is critical to resolve the dynamics of nonlinear wave–wave interactions in strongly sheared current fields.

Besides the wind, there are other drivers for surface ocean currents such as tides. In addition to the wind-driven current, the effect of the additional independent current on the wave group evolution is also studied. Our results show that adding the surface layer current in the same direction as the wave moves the focus point farther downstream and therefore increases the fetch and the wave height at the focus point.

The dynamics of airflow above a plunging breaking wave group is examined. In the presence of following wind, a shear layer of high vorticity separates from the breaking wave crest, remains detached while being coherent for some distance downstream, and then disintegrates into vortices. A recirculation zone is observed between the detached shear layer and the downwind side of the wave crest. This airflow structure is similar to that over a backward-facing step and a spilling breaker (Reul et al. 2008) as well as over young wind waves (Buckley and Veron 2016). After the plunging breaking, a strong clockwise vortex is formed at the crest and advected by the separation flow to a higher position.

In the presence of opposing wind, the airflow structure is similar to that over an airfoil at high angles of attack. The counterclockwise vortices shed from the detached shear layer above the rear face of the crest interact with the moving free surface in the opposite direction underneath and produce secondary vortices of opposite sign. Similar phenomena have been observed previously for a plunging breaker by Techet and McDonald (2005) and a modulated breaking wave group by Iafrati et al. (2013), without external wind forcing. It is conjectured that the formation of secondary vortices is dependent on the strength of the primary vortex and its distance and relative motion to the free surface. The strength of primary vortex for the opposing wind is much more pronounced than that for the following wind. This is due to the larger shear created by the wind and wave moving in the opposite direction and the blunt-shaped wave front face encountering the opposing wind. The primary vortices are advected downwind along the free surface and interact with the incoming wave crests and gradually lose their strength.

It is worth noting that the occurrence of similar airflow separation and vortex shedding but with smaller magnitude is observed for the nonbreaking wave group in Tian and Choi (2013). The presence of the steeper wave crest and the broken wave surface in a plunging breaking wave group greatly enhances the vorticity generation. These vortices downwind of the wave crest enhance the vertical mixing and momentum exchange just above the air–water interface.

The wind pressure distribution above the wave is largely in accordance with the wave crest geometry and the vorticity field of the airflow. We found that the presence of extreme waves greatly enhances the momentum and energy transfer at the air–water interface. The airflow separation causes large pressure drops in the leeward side of the crest and hence strongly affects the wind pressure and wave slope correlation and form drag. These results are consistent with experimental observations by Kharif et al. (2008) and Reul et al. (2008). Our results indicate that following wind imparts momentum to and increases the height of the wave through a positive form drag, while opposing wind extracts the momentum from and reduces the height of the wave through a negative form drag. The pressure distribution is far more complex than that predicted by Jeffreys' sheltering mechanism in the presence of extreme wave and breaking. The local surface pressure may well be affected by the airflow separation and vortex originated elsewhere and is not correlated well with the local wave.

Acknowledgments. The authors are grateful to Dr. Zhigang Tian for generously providing his experimental data and to Dr. John Richardson and Mr. Zhilong Liu for stimulating discussions. The authors gratefully acknowledge the support of the Physical Oceanography Program of the National Science Foundation under Award 1436642.

REFERENCES

Banner, M. L., 1990: The influence of wave breaking on the surface pressure distribution in wind–wave interactions. *J. Fluid Mech.*, **211**, 463–495, doi:10.1017/S0022112090001653.

——, and W. K. Melville, 1976: On the separation of air flow over water waves. *J. Fluid Mech.*, **77**, 825–842, doi:10.1017/S0022112076002905.

——, and W. L. Peirson, 1998: Tangential stress beneath wind-driven air–water interfaces. *J. Fluid Mech.*, **364**, 115–145, doi:10.1017/S0022112098001128.

——, and J. B. Song, 2002: On determining the onset and strength of breaking for deep water waves. Part II: Influence of wind forcing and surface shear. *J. Phys. Oceanogr.*, **32**, 2559–2570, doi:10.1175/1520-0485-32.9.2559.

Belcher, S. E., and J. C. R. Hunt, 1993: Turbulent shear flow over slowly moving waves. *J. Fluid Mech.*, **251**, 109–148, doi:10.1017/S0022112093003350.

——, and ——, 1998: Turbulent flow over hills and waves. *Annu. Rev. Fluid Mech.*, **30**, 507–538, doi:10.1146/annurev.fluid.30.1.507.

——, T. M. J. Newley, and J. C. R. Hunt, 1993: The drag on an undulating surface induced by the flow of a turbulent boundary layer. *J. Fluid Mech.*, **249**, 557–596, doi:10.1017/S0022112093001296.

Berberović, E., N. P. van Hinsberg, S. Jakirlić, I. V. Roisman, and C. Tropea, 2009: Drop impact onto a liquid layer of finite

thickness: Dynamics of the cavity evolution. *Phys. Rev.*, **79E**, 036306, doi:10.1103/PhysRevE.79.036306.

Buckley, M. P., and F. Veron, 2016: Structure of the airflow above surface waves. *J. Phys. Oceanogr.*, **46**, 1377–1397, doi:10.1175/JPO-D-15-0135.1.

Chambarel, J., C. Kharif, and O. Kimmoun, 2010: Generation of two-dimensional steep water waves on finite depth with and without wind. *Eur. J. Mech. B/Fluids*, **29**, 132–142, doi:10.1016/j.euromechflu.2009.12.002.

Chen, Q., J. M. Kaihatu, and P. A. Hwang, 2004: Incorporation of wind effects into Boussinesq wave models. *J. Waterw. Port Coastal Ocean Eng.*, **130**, 312–321, doi:10.1061/(ASCE)0733-950X(2004)130:6(312).

Dobson, F. W., 1971: Measurements of atmospheric pressure on wind-generated sea waves. *J. Fluid Mech.*, **48**, 91–127, doi:10.1017/S0022112071001496.

Donelan, M. A., A. V. Babanin, I. R. Young, and M. L. Banner, 2006: Wave-follower field measurements of the wind-input spectral function. Part II: Parameterization of the wind input. *J. Phys. Oceanogr.*, **36**, 1672–1689, doi:10.1175/JPO2933.1.

Elliott, J. A., 1972: Microscale pressure fluctuations near waves being generated by wind. *J. Fluid Mech.*, **54**, 427–448, doi:10.1017/S0022112072000783.

Fulgosi, M., D. Lakehal, S. Banerjee, and V. De Angelis, 2003: Direct numerical simulation of turbulence in a sheared air–water flow with a deformable interface. *J. Fluid Mech.*, **482**, 319–345, doi:10.1017/S0022112003004154.

Giovanangeli, J. P., C. Kharif, and E. Pelinovski, 2005: Experimental study of the wind effect on focusing of transient wave groups. *Proc. Rogue Waves 2004*, Brest, France, Ifremer, 2.1. [Available online at http://www.ifremer.fr/web-com/stw2004/rw/fullpapers/giovanangeli.pdf.]

Grare, L., L. Lenain, and W. K. Melville, 2013: Wave-coherent airflow and critical layers over ocean waves. *J. Phys. Oceanogr.*, **43**, 2156–2172, doi:10.1175/JPO-D-13-056.1.

Hara, T., and P. P. Sullivan, 2015: Wave boundary layer turbulence over surface waves in a strongly forced condition. *J. Phys. Oceanogr.*, **45**, 868–883, doi:10.1175/JPO-D-14-0116.1.

Hieu, P. D., P. N. Vinh, and N. T. Son, 2014: Study of wave-wind interaction at a seawall using a numerical wave channel. *Appl. Math. Modell.*, **38**, 5149–5159, doi:10.1016/j.apm.2014.04.038.

Hirt, C. W., and B. D. Nichols, 1981: Volume of fluid (VOF) method for dynamics of free boundaries. *J. Comput. Phys.*, **39**, 201–225, doi:10.1016/0021-9991(81)90145-5.

Hristov, T. S., S. D. Miller, and C. A. Friehe, 2003: Dynamical coupling of wind and ocean waves through wave-induced air flow. *Nature*, **422**, 55–58, doi:10.1038/nature01382.

Iafrati, A., A. Babanin, and M. Onorato, 2013: Modulational instability, wave breaking, and formation of large-scale dipoles in the atmosphere. *Phys. Rev. Lett.*, **110**, 184504, doi:10.1103/PhysRevLett.110.184504.

Jacobsen, N. G., D. R. Fuhrman, and J. Fredsøe, 2012: A wave generation toolbox for the open-source CFD library: OpenFoam. *Int. J. Numer. Methods Fluids*, **70**, 1073–1088, doi:10.1002/fld.2726.

Janssen, P. A., 1991: Quasi-linear theory of wind-wave generation applied to wave forecasting. *J. Phys. Oceanogr.*, **21**, 1631–1642, doi:10.1175/1520-0485(1991)021<1631:QLTOWW>2.0.CO;2.

Jasak, H., 1996: Error analysis and estimation for the finite volume method with applications to fluid flows. Ph.D. thesis, Imperial College London, 394 pp.

Jeffreys, H., 1925: On the formation of water waves by wind. *Philos. Trans. Roy. Soc. London*, **A107**, 189–206, doi:10.1098/rspa.1925.0015.

Kharif, C., and E. Pelinovsky, 2003: Physical mechanisms of the rogue wave phenomenon. *Eur. J. Mech. B/Fluids*, **22**, 603–634, doi:10.1016/j.euromechflu.2003.09.002.

——, J. P. Giovanangeli, J. Touboul, L. Grare, and E. Pelinovsky, 2008: Influence of wind on extreme wave events: Experimental and numerical approaches. *J. Fluid Mech.*, **594**, 209–247, doi:10.1017/S0022112007009019.

Kirby, J. T., and T. M. Chen, 1989: Surface waves on vertically sheared flows: Approximate dispersion relations. *J. Geophys. Res.*, **94**, 1013–1027, doi:10.1029/JC094iC01p01013.

Lakehal, D., M. Meier, and M. Fulgosi, 2002: Interface tracking towards the direct simulation of heat and mass transfer in multiphase flows. *Int. J. Heat Fluid Flow*, **23**, 242–257, doi:10.1016/S0142-727X(02)00172-8.

Lin, M. Y., C. H. Moeng, W. T. Tsai, P. P. Sullivan, and S. E. Belcher, 2008: Direct numerical simulation of wind-wave generation processes. *J. Fluid Mech.*, **616**, 1–30, doi:10.1017/S0022112008004060.

Liu, K., Q. Chen, and J. M. Kaihatu, 2015: Modeling wind effects on shallow water waves. *J. Waterw. Port Coastal Ocean Eng.*, **142**, 04015012, doi:10.1061/(ASCE)WW.1943-5460.0000314.

Longo, S., D. Liang, L. Chiapponi, and L. A. Jiménez, 2012: Turbulent flow structure in experimental laboratory wind-generated gravity waves. *Coastal Eng.*, **64**, 1–15, doi:10.1016/j.coastaleng.2012.02.006.

Lv, X., Q. Zou, and D. Reeve, 2009: An unstructured 3D LES solver for free surface flow and breaking waves. *Int. J. Offshore Polar Eng.*, **19**, 308–316.

——, ——, Y. Zhao, and D. Reeve, 2010: A novel coupled level set and volume of fluid method for sharp interface capturing on 3D tetrahedral grids. *J. Comput. Phys.*, **229**, 2573–2604, doi:10.1016/j.jcp.2009.12.005.

——, ——, ——, and ——, 2012: A preconditioned implicit free-surface capture scheme for large density ratio on tetrahedral grids. *Commun. Comput. Phys.*, **11**, 215–248, doi:10.4208/cicp.170510.290311a.

Miles, J. W., 1957: On the generation of surface waves by shear flows. *J. Fluid Mech.*, **3**, 185–204, doi:10.1017/S0022112057000567.

——, 1962: On the generation of surface waves by shear flows. Part 4. *J. Fluid Mech.*, **13**, 433–448, doi:10.1017/S0022112062000828.

——, 1993: Surface-wave generation revisited. *J. Fluid Mech.*, **256**, 427–441, doi:10.1017/S0022112093002836.

Mitsuyasu, H., and T. Honda, 1982: Wind-induced growth of water waves. *J. Fluid Mech.*, **123**, 425–442, doi:10.1017/S0022112082003139.

——, and Y. Yoshida, 2005: Air-sea interactions under the existence of opposing swell. *J. Oceanogr.*, **61**, 141–154, doi:10.1007/s10872-005-0027-1.

Moreira, R. M., and J. T. A. Chacaltana, 2015: Vorticity effects on nonlinear wave–current interactions in deep water. *J. Fluid Mech.*, **778**, 314–334, doi:10.1017/jfm.2015.385.

Mori, N., P. C. Liu, and T. Yasuda, 2002: Analysis of freak wave measurements in the Sea of Japan. *Ocean Eng.*, **29**, 1399–1414, doi:10.1016/S0029-8018(01)00073-7.

Ning, D. Z., X. L. Zhuo, T. C. Hou, and B. Teng, 2015: Numerical investigation of focused waves on uniform currents. *Int. J. Offshore Polar Eng.*, **25**, 19–25.

Nwogu, O., 2009: Interaction of finite-amplitude waves with vertically sheared current fields. *J. Fluid Mech.*, **627**, 179–213, doi:10.1017/S0022112009005850.

Peirson, W. L., and M. L. Banner, 2003: Aqueous surface layer flows induced by microscale breaking wind waves. *J. Fluid Mech.*, **479**, 1–38, doi:10.1017/S0022112002003336.

——, and A. W. Garcia, 2008: On the wind-induced growth of slow water waves of finite steepness. *J. Fluid Mech.*, **608**, 243–274, doi:10.1017/S002211200800205X.

Perlin, M., W. Choi, and Z. Tian, 2013: Breaking waves in deep and intermediate waters. *Annu. Rev. Fluid Mech.*, **45**, 115–145, doi:10.1146/annurev-fluid-011212-140721.

Phillips, O. M., 1957: On the generation of waves by turbulent wind. *J. Fluid Mech.*, **2**, 417–445, doi:10.1017/S0022112057000233.

——, 1977: *Dynamics of the Upper Ocean.* Cambridge University Press, 336 pp.

——, and M. L. Banner, 1974: Wave breaking in the presence of wind drift and swell. *J. Fluid Mech.*, **66**, 625–640, doi:10.1017/S0022112074000413.

Plant, W. J., 1982: A relationship between wind stress and wave slope. *J. Geophys. Res.*, **87**, 1961–1967, doi:10.1029/JC087iC03p01961.

Reul, N., H. Branger, and J. P. Giovanangeli, 1999: Air flow separation over unsteady breaking waves. *Phys. Fluids*, **11**, 1959–1961, doi:10.1063/1.870058.

——, ——, and ——, 2008: Air flow structure over short-gravity breaking water waves. *Bound.-Layer Meteor.*, **126**, 477–505, doi:10.1007/s10546-007-9240-3.

Rusche, H., 2002: Computational fluid dynamics of dispersed two-phase flows at high phase fractions. Ph.D. thesis, Imperial College London, 343 pp.

Savelyev, I. B., B. K. Haus, and M. A. Donelan, 2011: Experimental study on wind-wave momentum flux in strongly forced conditions. *J. Phys. Oceanogr.*, **41**, 1328–1344, doi:10.1175/2011JPO4577.1.

Scardovelli, R., and S. Zaleski, 1999: Direct numerical simulation of free-surface and interfacial flow. *Annu. Rev. Fluid Mech.*, **31**, 567–603, doi:10.1146/annurev.fluid.31.1.567.

Sethian, J. A., and P. Smereka, 2003: Level set methods for fluid interfaces. *Annu. Rev. Fluid Mech.*, **35**, 341–372, doi:10.1146/annurev.fluid.35.101101.161105.

Siddiqui, M. K., and M. R. Loewen, 2007: Characteristics of the wind drift layer and microscale breaking waves. *J. Fluid Mech.*, **573**, 417–456, doi:10.1017/S0022112006003892.

Smagorinsky, J., 1963: General circulation experiments with the primitive equations: I. The basic experiment. *Mon. Wea. Rev.*, **91**, 99–164, doi:10.1175/1520-0493(1963)091<0099:GCEWTP>2.3.CO;2.

Snyder, R. L., F. W. Dobson, J. A. Elliott, and R. B. Long, 1981: Array measurements of atmospheric pressure fluctuations above surface gravity waves. *J. Fluid Mech.*, **102**, 1–59, doi:10.1017/S0022112081002528.

Sullivan, P. P., J. C. McWilliams, and C. H. Moeng, 2000: Simulation of turbulent flow over idealized water waves. *J. Fluid Mech.*, **404**, 47–85, doi:10.1017/S0022112099006965.

——, ——, and W. K. Melville, 2007: Surface gravity wave effects in the oceanic boundary layer: Large-eddy simulation with vortex force and stochastic breakers. *J. Fluid Mech.*, **593**, 405–452, doi:10.1017/S002211200700897X.

——, J. B. Edson, T. Hristov, and J. C. McWilliams, 2008: Large-eddy simulations and observations of atmospheric marine boundary layers above nonequilibrium surface waves. *J. Atmos. Sci.*, **65**, 1225–1245, doi:10.1175/2007JAS2427.1.

Sussman, M., K. M. Smith, M. Y. Hussaini, M. Ohta, and R. Zhi-Wei, 2007: A sharp interface method for incompressible two-phase flows. *J. Comput. Phys.*, **221**, 469–505, doi:10.1016/j.jcp.2006.06.020.

Techet, A. H., and A. K. McDonald, 2005: High speed PIV of breaking waves on both sides of the air-water interface. *Sixth Int. Symp. on Particle Image Velocimetry*, Pasadena, CA, Institute of Physics, 1–14.

Tian, Z., and W. Choi, 2013: Evolution of deep-water waves under wind forcing and wave breaking effects: Numerical simulations and experimental assessment. *Eur. J. Mech. B/Fluids*, **41**, 11–22, doi:10.1016/j.euromechflu.2013.04.001.

——, M. Perlin, and W. Choi, 2010: Observation of the occurrence of air flow separation over water waves. *Proc. 29th Int. Conf. on Ocean, Offshore and Arctic Engineering*, Shanghai, China, ASME, 333–341, doi:10.1115/OMAE2010-20576.

Touboul, J., J. P. Giovanangeli, C. Kharif, and E. Pelinovsky, 2006: Freak waves under the action of wind: Experiments and simulations. *Eur. J. Mech. B/Fluids*, **25**, 662–676, doi:10.1016/j.euromechflu.2006.02.006.

Tsuruya, H., S. Yanagishima, and Y. Matsunobu, 1985: Decay of mechanically generated waves in an opposing wind. Rep. of the Port and Harbor Research Institute, PARI Rep. 024-03-02, 31–72. [Available online at http://www.pari.go.jp/search-pdf/vol024-no03-02.pdf.]

Wang, Z., Q.-P. Zou, and D. Reeve, 2009: Simulation of spilling breaking waves using a two phase flow CFD model. *Comput. Fluids*, **38**, 1995–2005, doi:10.1016/j.compfluid.2009.06.006.

Weissman, M. A., 1986: Observations and measurements of air flow over water waves. *Wave Dynamics and Radio Probing of the Ocean Surface*, Springer, 335–352, doi:10.1007/978-1-4684-8980-4_24.

Weller, H. G., 2005: Derivation, modelling and solution of the conditionally averaged two-phase flow equations. OpenCFD Ltd. Tech. Rep. TR/HGW/02, 29 pp.

——, G. Tabor, H. Jasak, and C. Fureby, 1998: A tensorial approach to computational continuum mechanics using object-oriented techniques. *Comput. Phys.*, **12**, 620–631, doi:10.1063/1.168744.

Wu, J., 1975: Wind-induced drift currents. *J. Fluid Mech.*, **68**, 49–70, doi:10.1017/S0022112075000687.

Xie, Z., 2014: Numerical modelling of wind effects on breaking solitary waves. *Eur. J. Mech. B/Fluids*, **43**, 135–147, doi:10.1016/j.euromechflu.2013.08.001.

Yan, S., and Q. W. Ma, 2010: Numerical simulation of interaction between wind and 2D freak waves. *Eur. J. Mech. B/Fluids*, **29**, 18–31, doi:10.1016/j.euromechflu.2009.08.001.

——, and ——, 2011: Improved model for air pressure due to wind on 2D freak waves in finite depth. *Eur. J. Mech. B/Fluids*, **30**, 1–11, doi:10.1016/j.euromechflu.2010.09.005.

——, and ——, 2012: Numerical study on significance of wind action on 2-D freak waves with different parameters. *J. Mar. Sci. Technol.*, **20**, 9–17. [Available online at http://openaccess.city.ac.uk/id/eprint/4296.]

Yang, D., and L. Shen, 2010: Direct-simulation-based study of turbulent flow over various waving boundaries. *J. Fluid Mech.*, **650**, 131–180, doi:10.1017/S0022112009993557.

——, and ——, 2011: Simulation of viscous flows with undulatory boundaries: Part II. Coupling with other solvers for two-fluid computations. *J. Comput. Phys.*, **230**, 5510–5531, doi:10.1016/j.jcp.2011.02.035.

Zhang, Y., Q.-P. Zou, and D. Greaves, 2010a: Numerical simulation of free-surface flow using the level-set method with global mass correction. *Int. J. Numer. Methods Fluids*, **63**, 651–680, doi:10.1002/fld.2090.

——, ——, ——, D. Reeve, A. Hunt-Raby, D. Graham, P. James, and X. Lv, 2010b: A level set immersed boundary method for water entry and exit. *Commun. Comput. Phys.*, **8**, 265–288, doi:10.4208/cicp.060709.060110a.

Zou, Q.-P., 1995: A viscoelastic model for turbulent flow over undulating topography and progressive waves. Ph.D. thesis, Scripps Institution of Oceanography, University of California, San Diego, 91 pp.

——, 1998: A viscoelastic model for turbulent flow over an undulating topography. *J. Fluid Mech.*, **355**, 81–112, doi:10.1017/S0022112097007386.

——, and H. Chen, 2016: Numerical simulation of wind effects on the evolution of freak waves. *Proc. 26th Int. Ocean and Polar Engineering Conf.*, Rhodes, Greece, ISOPE, 635–640. [Available online at https://www.onepetro.org/conference-paper/ISOPE-I-16-055.]